Applied Catalysis B: Environment and Energy 400 (2027) 127265

Contents lists available at ScienceDirect

Applied Catalysis B: Environment and Energy

journal homepage: www.elsevier.com/locate/apcatb

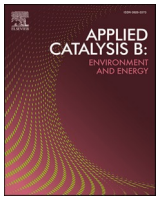

Yb-modulated ultrathin Fe-NDC nanoplates for ampere-level water electrolysis

Sheraz Muhammad [a], Sumayya Khan [a], Sana Zahoor [a], Rahmat Ullah [a], Ali Aman [a], Tayirjan Taylor Isimjan [b,*], Shohreh Azizi [c], Xiulin Yang [a,*]

[a] Guangxi Key Laboratory of Low Carbon Energy Materials, School of Chemistry and Pharmaceutical Sciences, Guangxi Normal University, Guilin 541004, China
[b] Saudi Arabia Basic Industries Corporation (SABIC) at King Abdullah University of Science and Technology (KAUST), Thuwal 23955-6900, Saudi Arabia
[c] UNESCO-UNISA Africa Chair in Nanosciences/Nanotechnology, College of Graduate Studies, University of South Africa, Muckleneuk Ridge, Pretoria 0181, South Africa

ARTICLE INFO

Keywords:
Yb-doped Fe-NDC
Oxygen evolution reaction
Operando spectroscopy
Adsorbate evolution mechanism
Overall water splitting

ABSTRACT

Developing efficient and durable non-noble-metal electrocatalysts for alkaline oxygen evolution reaction (OER) is essential for advancing water electrolysis technologies. Herein, we report a two-dimensional (2D) ytterbium-doped Fe-NDC metal-organic framework ($Yb_{0.4}$Fe-NDC) directly grown on nickel foam via a one-step solvothermal strategy. Benefiting from ultrathin nanoplate morphology and Yb-induced electronic modulation, $Yb_{0.4}$Fe-NDC delivers low overpotentials of 271 mV at 200 mA cm^{-2}, together with a low Tafel slope of 48 mV dec^{-1} and stable operation over 100 h. *Operando* Raman spectroscopy reveals earlier formation of active FeOOH species, while *operando* ATR-FTIR identifies the *OOH intermediate, confirming an adsorbate evolution mechanism (AEM) pathway. Density functional theory calculations show that Yb incorporation shifts the Fe D-band center upward from −1.45 to −1.39 eV, strengthens Fe–*OOH interaction, and lowers the free-energy barrier for *OOH formation from 1.77 to 1.65 eV. In a two-electrode electrolyzer, the $Yb_{0.4}$Fe-NDC$^{(+)}||^{(-)}$Pt/C system achieves low cell voltages of 1.57 and 1.64 V at 200 and 400 mA cm^{-2}, respectively, with stable operation for 160 and 128 h. Furthermore, in anion exchange membrane water electrolyzer (AEMWE), it delivers a cell voltage of 2.44 V at 1.0 A cm^{-2} at 25 °C and 2.19 V at 60 °C, with stable operation for over 100 h. These findings highlight rare-earth electronic modulation as an effective strategy for designing high-performance MOF-based OER electrocatalysts with promising practical potential.

1. Introduction

Developing efficient and sustainable energy technologies is essential to achieve carbon neutrality and meet increasing global energy demands [1,2]. Water electrolysis offers a promising route for producing storable and carbon-neutral hydrogen through two half-reactions: the hydrogen evolution reaction (HER) at the cathode and the oxygen evolution reaction (OER) at the anode [3,4]. Among the various water electrolysis technologies, alkaline anion exchange membrane water electrolyzers (AEMWE) stand out as a promising platform, offering the benefits of a zero-gap cell configuration and compatibility with dilute KOH electrolytes, which together enable cost-effective and scalable hydrogen production [5]. However, operating AEMWE systems at high-current densities (ampere level) imposes rigorous requirements on the catalytic performance and long-term stability of electrode materials [6]. Benchmark OER catalysts based on IrO_2 and RuO_2 exhibit excellent catalytic activity but suffer from high cost, limited abundance, and poor stability under alkaline conditions [7]. Moreover, the OER involves sluggish four-electron transfer kinetics, which remains the major bottleneck in overall water splitting efficiency. Therefore, the development of non-precious-metal electrocatalysts with high activity and long-term durability is crucial for advancing AEMWE technology toward scalable green hydrogen production. In this regard, various transition metal-based materials, including chalcogenides, selenides, oxides, phosphides, tellurides, nitrides, and MOFs, have attracted significant attention as OER electrocatalysts [8]. Among these candidates, MOFs hybrid organic-inorganic crystalline materials are particularly attractive owing to their high surface area, tunable porosity, diverse metal centers, and tailorable functional groups [9–11]. Their modular architectures further enable rational catalyst design through the deliberate selection

* Corresponding authors.
E-mail addresses: isimjant@sabic.com (T.T. Isimjan), xlyang@gxnu.edu.cn (X. Yang).

https://doi.org/10.1016/j.apcatb.2026.127265
Received 29 May 2026; Received in revised form 21 July 2026; Accepted 21 July 2026
Available online 23 July 2026

of metal nodes and organic ligands [12–14]. Nevertheless, pristine MOFs generally suffer from poor electrical conductivity and insufficient long-term stability under harsh electrochemical conditions, severely limiting their practical application in high-current-density water electrolysis [15–17]. Overcoming these intrinsic limitations while maintaining structural advantages remains a major challenge.

To address these issues, various strategies, including ligand engineering, elemental doping, and interface modulation, have been extensively explored [18–21]. In particular, Fe-based MOF electrocatalysts are known to undergo dynamic surface reconstruction under alkaline OER conditions, typically forming an amorphous Fe oxyhydroxide (FeOOH) layer that serves as the catalytically active phase [22–24]. Although such reconstruction is generally beneficial for improving intrinsic activity, excessive reconstruction can induce framework collapse, accelerated metal dissolution, and loss of structural integrity, thereby compromising long-term durability [25,26]. Recent studies have suggested that controlled or partial reconstruction, in which the parent MOF framework is largely preserved while a thin oxyhydroxide layer is generated on the surface, offers an effective strategy to simultaneously enhance catalytic activity and structural stability [27]. In this context, heteroatom doping has emerged as a promising approach not only for tuning the electronic structure but also for regulating the reconstruction behavior by strengthening the metal-ligand coordination environment and suppressing excessive metal leaching. However, most prior studies attribute the performance enhancement of doped Fe-MOFs solely to electronic structure modulation, without considering whether the dopant simultaneously influences the dynamic reconstruction pathway. This narrow focus overlooks the potential of dopants to dual-functionally modulate both electronic properties and structural evolution during OER.

Rare-earth elements are particularly attractive because of their unique electronic configurations, strong oxophilicity, and flexible coordination chemistry. Incorporating rare-earth species into MOFs can effectively regulate their electronic structures, optimize charge redistribution, introduce additional electroactive sites, and potentially stabilize the catalyst framework during electrochemical reconstruction, thereby accelerating OER kinetics while improving durability [28]. In particular, ytterbium (Yb), with its unique 4 f electronic structure, is expected to strongly influence the electronic environment of neighboring transition-metal centers and modulate adsorption energetics of oxygenated intermediates [29]. For example, *Liao et al.* reported a Ce-doped Co-MOF nanoflower exhibiting an overpotential of 267 mV at 10 mA cm^{-2} and attributed the enhanced activity to Co-O-Ce orbital coupling [30]. Similarly, *Ma et al.* demonstrated that a Dy-doped Fe-MOF achieved a low overpotential of 318 mV at 500 mA cm^{-2} due to electron donation from Dy to neighboring Fe centers [31]. Despite these advances, several critical gaps persist in rare-earth-doped MOF electrocatalysts for OER. Most reported systems are limited to low current densities and lack well-defined 2D nanostructures that maximize active site exposure features critical for achieving high current densities in practical applications. Moreover, the role of rare-earth dopants has been primarily interpreted through static electronic modulation, while their potential to dynamically regulate the reconstruction behavior of Fe-based MOFs under alkaline OER conditions remains unexplored. Critically, the translation from half-cell catalyst performance to practical AEMWE operating at ampere-level current densities has rarely been demonstrated. In particular, Yb-doped Fe-NDC with a 2D ultrathin nanoplate architecture has not yet been reported for OER, and the dual role of Yb in simultaneously tuning the electronic structure, Fe valence state, adsorption energetics, and reconstruction stability of the MOF scaffold remains entirely unclear. Thus, a comprehensive investigation bridging controlled synthesis, *operando* mechanistic understanding, and practical AEMWE deployment is urgently needed to advance rare-earth-engineered MOF electrocatalysts toward scalable green hydrogen production.

In this work, we report a 2D Yb-doped Fe-NDC electrocatalyst for highly efficient OER under high-current-density conditions relevant to practical water electrolysis. The ultrathin nanoplate architecture facilitates exposure of active sites and accelerates mass transport, while Yb incorporation modulates the electronic environment of Fe centers through interfacial electronic coupling. Combined *operando* spectroscopic analysis and DFT calculations reveal that Yb doping elevates the Fe D-band center, strengthens *OOH adsorption, and lowers the free-energy barrier for *OOH formation, thereby promoting the adsorbate evolution mechanism (AEM) pathway. The optimized $Yb_{0.4}$Fe-NDC catalyst delivers a low overpotential of 271 mV at 200 mA cm^{-2} and maintains stable operation for more than 100 h. In a two-electrode electrolyzer configuration ($Yb_{0.4}$Fe-NDC$^{(+)}$||$^{(-)}$Pt/C), a cell voltage of 1.64 V at 400 mA cm^{-2} is sustained for over 128 h, outperforming many previously reported Fe-based MOF electrocatalysts under comparable conditions. Furthermore, in AEMWE it delivers a cell voltage of 2.44 V at 1.0 A cm^{-2} at 25 °C and 2.19 V at 60 °C, with stable operation for over 100 h at 1.0 A cm^{-2}. This work highlights the effectiveness of rare-earth engineering for constructing high-performance MOF electrocatalysts and provides mechanistic insights into electronic modulation strategies for high-current-density water oxidation.

2. Experimental section

2.1. Materials

Iron(III) nitrate nonahydrate ($Fe(NO_3)_3{\cdot}9\ H_2O$, > 99%), ytterbium (III) nitrate pentahydrate ($Yb(NO_3)_3{\cdot}5\ H_2O$, > 99%), and 1,4-naphthalenedicarboxylic acid (NDC, >99%) were employed as metal and organic precursors. Solvents such as ethanol (>99.7%), N,N-dimethylformamide (DMF, >99%), and deionized (DI) water were obtained from Xilong Science Co., Ltd. Additional reagents, such as sulfuric acid (H_2SO_4, 37%) and potassium hydroxide (KOH, >90%), were also used. Ruthenium(III) chloride hydrate ($RuCl_3{\cdot}xH_2O$) was purchased from Shanghai Macklin Chemical Reagent Co., Ltd. RuO_2 powder was subsequently prepared by calcining $RuCl_3$ in air at 400 °C. Nickel foam (NF, 1.6 mm thickness), used as the electrode substrate, was obtained from Guang Sheng Jia New Materials Co., Ltd., and cut into 2 cm × 4 cm pieces for experimental use. Commercial Pt/C (20 wt%) and Nafion solution (5 wt%) were supplied by Suzhou Sinero Technology Co., Ltd. All reagents were of analytical grade and used as received without additional purification.

2.2. Synthesis of Fe-NDC

In a typical synthesis, 1.0 mmol of $Fe(NO_3)_3{\cdot}9\ H_2O$ and 1.5 mmol of NDC were dissolved in a mixed solvent composed of 25 mL of DMF, 5 mL of deionized water, and 5 mL of ethanol. The mixture was sonicated for 25 min to obtain a homogeneous precursor solution. A piece of nickel foam (NF, 2 × 4 cm) was cleaned prior to use by sequential sonication in 0.5 M H_2SO_4, ethanol, and deionized water for 10 min each, followed by drying under vacuum. The cleaned NF was immersed into the precursor solution, and the assembly was transferred into a Teflon-lined stainless-steel autoclave. The autoclave was heated at 125 °C for 8 h and then allowed to cool naturally to room temperature. The resulting electrode was washed with ethanol and dried at 60 °C overnight. The mass loading of Fe-NDC on NF is approximately 3.7 mg cm^{-2}.

2.3. Synthesis of Yb-doped Fe-NDC

The synthesis of Yb-doped Fe-NDC followed a similar procedure with the addition of an Yb precursor. A solution (A) containing 1.0 mmol of $Fe(NO_3)_3{\cdot}9\ H_2O$ and 1.5 mmol of NDC was prepared in 25 mL of DMF, 5 mL of deionized water, and 5 mL of ethanol, and sonicated for 25 min. Separately, a solution (B) was prepared by dissolving a desired amount of $Yb(NO_3)_3{\cdot}5\ H_2O$ (0.2, 0.4, or 0.6 mmol) in 15 mL of deionized water. Solutions A and B were mixed thoroughly, and a cleaned NF substrate (cleaned as described above) was immersed into the combined mixture.

The assembly was transferred into a Teflon-lined autoclave and heated at 125 °C for 8 h. After natural cooling, the sample was washed with ethanol and dried at 60 °C overnight, yielding Yb×Fe-NDC/NF. The mass loadings of $Yb_{0.2}$Fe-NDC, $Yb_{0.4}$Fe-NDC, and $Yb_{0.6}$Fe-NDC were determined to be 3.5, 4.1, and 4.5 mg cm^{-2}, respectively.

2.4. Preparation of working electrode for comparison

For benchmarking, Pt/C and RuO_2 working electrodes were prepared via a simple drop-casting method. In a typical procedure, 2.0 mg of 20 wt% Pt/C or RuO_2 powder was dispersed in a mixture of 220 μL DI water and ethanol, followed by the addition of 5 μL of 5 wt% Nafion solution. The suspension was ultrasonicated for 30 min to achieve a uniform dispersion. The resulting catalyst ink was then drop-cast onto pre-cleaned NF substrates (1 cm × 1 cm) and allowed to dry under ambient conditions before electrochemical testing.

3. Results and discussion

3.1. Structural characterization of materials

The fabrication process of the Yb-doped Fe-NDC electrode is schematically illustrated in Fig. 1a. A one-step solvothermal approach enables the direct growth of ultrathin Yb-doped Fe-NDC nanoplates on nickel foam (NF) through the simultaneous incorporation of Yb into the Fe-NDC framework. The Fe-NDC metal-organic framework is constructed from Fe ions coordinated to NDC linkers. Each carboxylate group of the naphthalene ring binds to metal centers in a bidentate bridging mode. In the pristine Fe-NDC structure, the Fe ion is six-coordinated (octahedral FeO_6), bonded to oxygen atoms of the NDC carboxylate groups [32–35]. The introduction of Yb modifies the local electronic environment and coordination characteristics, forming Fe-O-Yb bridging motifs without disrupting the overall framework topology. Such coordination interactions influence nucleation and crystal growth behavior, ultimately contributing to the formation of ultrathin 2D nanoplates. The larger ionic radius of Yb induces local lattice distortion, but the basic octahedral coordination geometry of the Fe centers is retained [36]. As a result, incorporating Yb into the Fe and NDC precursor solution leads to a well-defined nanoplate morphology. The X-ray diffraction (XRD) patterns (Fig. 1b) show that all catalysts exhibit a characteristic diffraction peak at approximately $2\theta = 8.41°$, consistent with the simulated Fe-NDC pattern (CCDC#2214948), thereby confirming successful formation of the MOF structure on the NF substrate [37]. As the Yb content increases from 0 to 0.6 mM, the intensity of this diffraction peak gradually decreases, indicating that higher doping levels induce slight structural distortion while preserving the overall MOF framework. No additional impurity peaks associated with Yb-based crystalline phases are detected, suggesting successful incorporation of Yb species into the Fe-NDC framework without phase segregation. Fourier transform infrared (FTIR) spectroscopy was further employed to probe the coordination environment and functional groups (Fig. 1c). A broad absorption band observed at 3300–3500 cm^{-1} is assigned to the stretching vibration of carboxylic O-H groups, suggesting the presence of hydrogen-bonded hydroxyl species within the framework. The peaks located in the 1200–1600 cm^{-1} region correspond to the stretching vibrations of C═O, aromatic C═C, and COO groups derived from the NDC ligand, confirming successful coordination between the organic linker and metal centers. The band at 783 cm^{-1} is attributed to C-H vibrations, whereas the low-frequency peak at 493 cm^{-1} originates from metal-oxygen (M-O) or M-O-M bonding vibrations, further

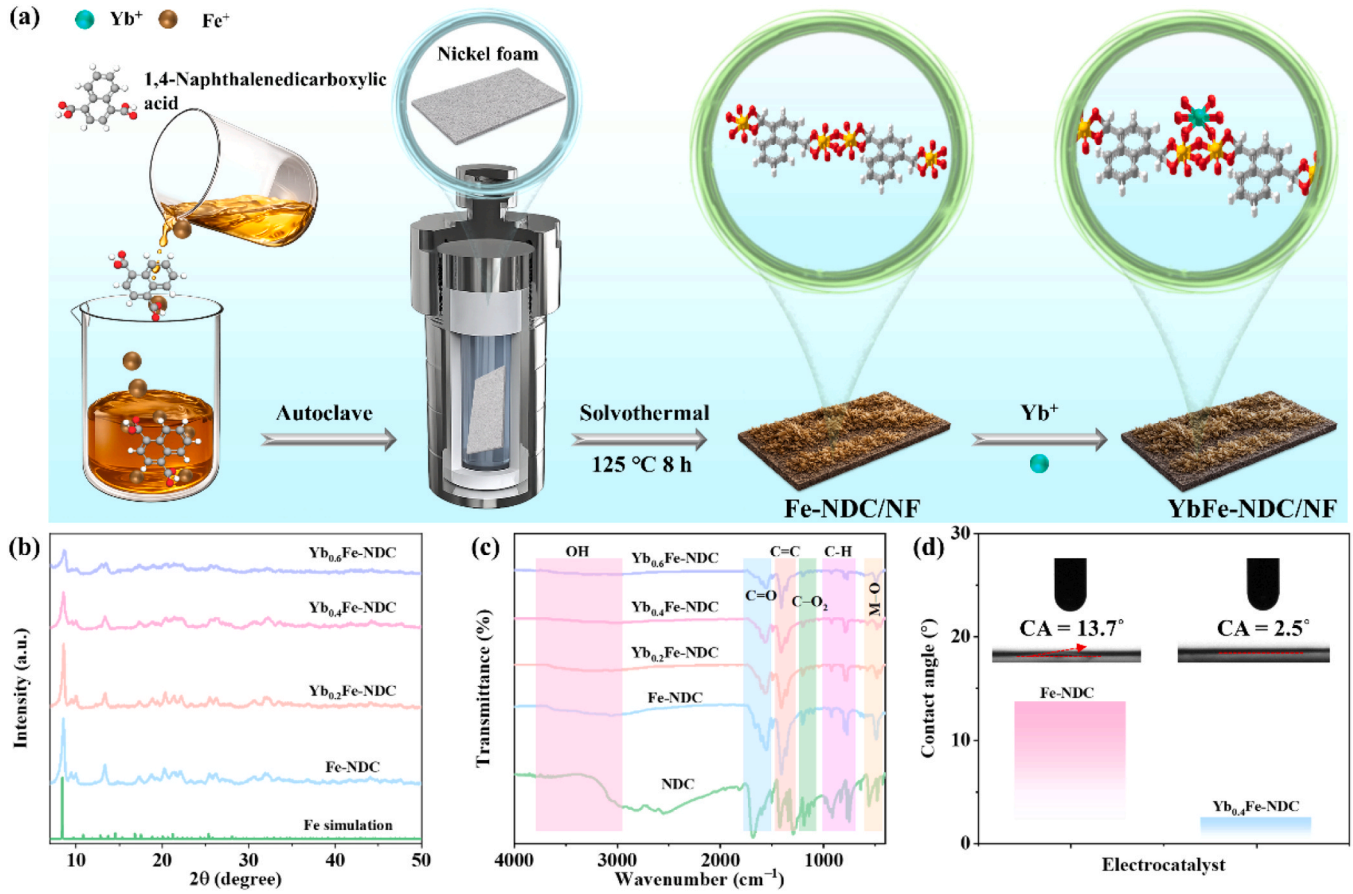

Fig. 1. Synthesis and structural analysis. (a) Schematic illustration of the synthesis of 2D Yb_xFe-NDC nanoplates. (b) XRD patterns of all prepared electrocatalysts together with the simulated pattern. (c) FTIR spectra of the NDC ligand and all synthesized catalysts. (d) Contact angle measurements of Fe-NDC and $Yb_{0.4}$Fe-NDC.

supporting the formation of coordinated metal-ligand structures [38–40]. Notably, the Yb-doped samples display nearly identical FTIR profiles to pristine Fe-NDC, indicating that Yb incorporation does not significantly alter the coordination environment of the NDC ligand and is effectively accommodated within the original framework. The surface wettability of the catalysts was evaluated through water contact angle measurements (Fig. 1d). Pristine Fe-NDC exhibits a contact angle of 13.7°, indicative of a hydrophilic surface. Upon Yb doping, the contact angle decreases progressively, with $Yb_{0.2}$Fe-NDC (7.8°), $Yb_{0.4}$Fe-NDC (2.5°), and $Yb_{0.6}$Fe-NDC (4.1°) showing substantially enhanced hydrophilicity (Fig. S1). The lowest contact angle observed for $Yb_{0.4}$Fe-NDC (2.5°) indicates optimal surface wettability, while a slight increase at higher Yb content suggests that excessive doping may marginally reduce hydrophilicity. Such improved wettability is highly advantageous for electrocatalytic operation at high current densities because it facilitates electrolyte infiltration, accelerates gas bubble release, and improves reactant accessibility to active sites, thereby contributing to the enhanced OER performance of $Yb_{0.4}$Fe-NDC [41,42].

Scanning electron microscopy (SEM) images reveal the 2D morphology of the synthesized materials. Pristine Fe-NDC (Fig. 2a) exhibits uniform coverage of interconnected 2D nanoplates on the nickel foam NF [43,44]. After Yb incorporation (Fig. 2b and Figs. S2a-b), the catalyst maintains a similar nanoplate morphology, indicating that Yb doping does not disrupt the overall structural architecture of the Fe-NDC framework. Transmission electron microscopy (TEM) further confirms the formation of ultrathin 2D nanoplates (Fig. 2c). The high transparency of the nanoplates suggests nanoscale thickness, which is advantageous for exposing abundant accessible active sites and facilitating mass transport during electrocatalysis. High-resolution TEM (HR-TEM) analysis of $Yb_{0.4}$Fe-NDC (Fig. 2d) does not show distinct lattice fringes, likely owing to the electron-beam sensitivity of MOFs, where weak metal-ligand coordination and structural flexibility can induce amorphization under irradiation [45]. Consistently, the selected-area electron diffraction (SAED) pattern (Fig. 2e) displays diffuse rings without discernible diffraction spots, further supporting partial amorphization during electron-beam exposure [46]. The surface morphology and thickness of the nanoplates were further characterized by atomic force microscopy (AFM). As shown in Fig. 2f, the AFM image exhibits distinct height variations across the nanoplates surface. Corresponding height profiles reveal an average thickness of approximately 3.53 nm (Fig. 2g), confirming the ultrathin nature of the 2D architecture. Such a thin nanoplate structure can maximize exposed active surface area and shorten charge/mass transport pathways, thereby favoring electrocatalytic OER kinetics. The elemental composition and spatial distribution were subsequently investigated using high-angle annular dark-field scanning transmission electron microscopy (HAADF-STEM) coupled with energy-dispersive X-ray spectroscopy (EDS) mapping (Fig. 2h-l). The HAADF-STEM image clearly demonstrates the ultrathin nanoplate morphology, while EDS elemental mapping confirms the homogeneous distribution of C, O, Fe, and Yb throughout the nanoplate. Furthermore, the corresponding EDS spectrum (Fig. S3) displays characteristic signals of C and O from the NDC linker together with Fe and Yb peaks, confirming successful incorporation of Yb into the Fe-NDC framework.

Thermogravimetric analysis (TGA) and derivative thermogravimetry (DTG) were performed to evaluate the thermal stability and decomposition behavior of the catalysts (Fig. 3a-b). For $Yb_{0.4}$Fe-NDC, four distinct weight-loss stages are observed. The initial weight loss of 5.7%

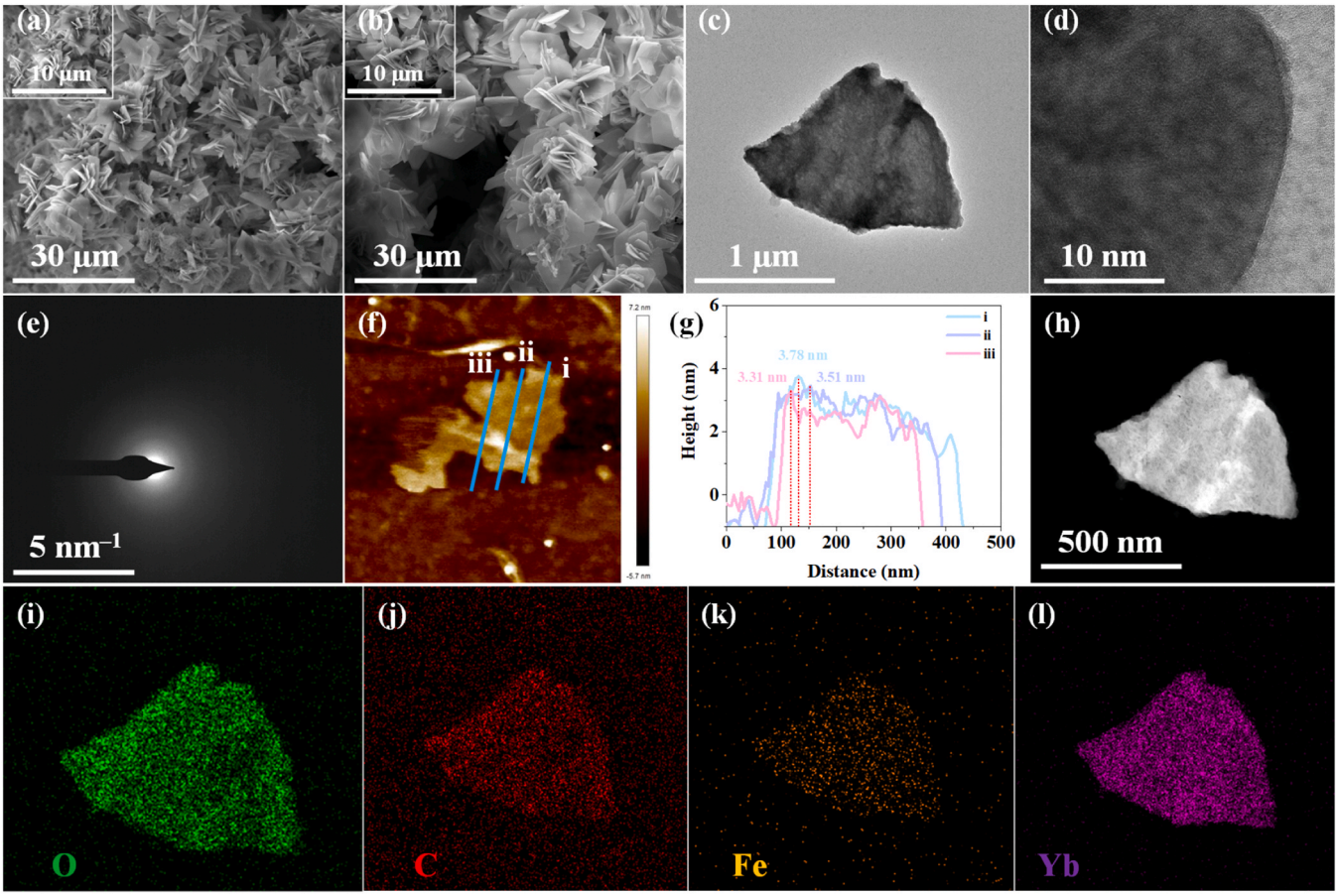

Fig. 2. Microstructure analysis. (a) SEM images of Fe-NDC and (b) $Yb_{0.4}$Fe-NDC. (c) TEM, (d) High-resolution-TEM, (e) SAED pattern, (f) AFM, (g) height profile, (h) HAADF-STEM image and (i-l) corresponding elemental mapping images of 2D $Yb_{0.4}$Fe-NDC nanoplates.

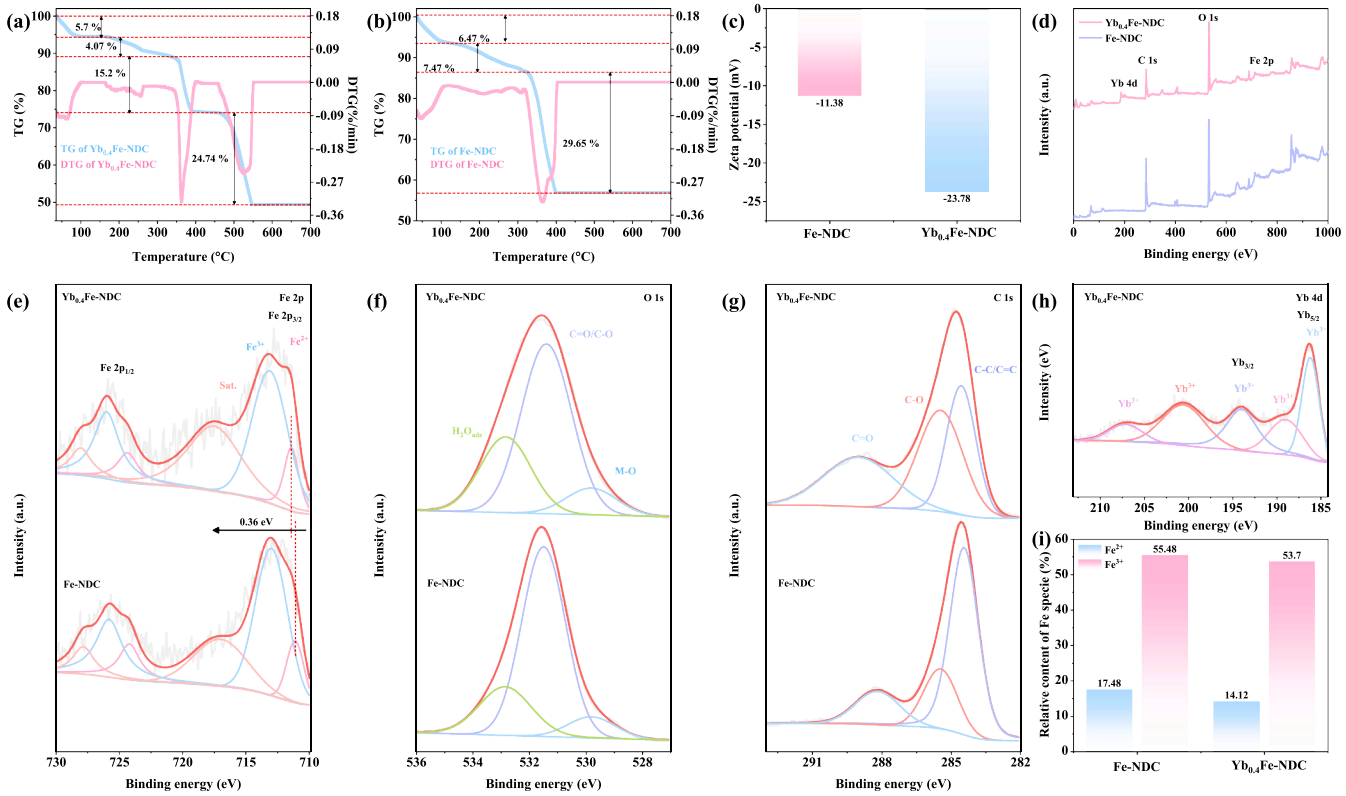

Fig. 3. (a) TG/DTG curves of $Yb_{0.4}$Fe-NDC and (b) Fe-NDC. (c) Zeta potential of Fe-NDC and $Yb_{0.4}$Fe-NDC. High-resolution XPS spectra of Fe-NDC and $Yb_{0.4}$Fe-NDC: (d) Survey, (e) Fe 2p, (f) O 1 s, (g) C 1 s and (h) Yb 4d. (i) Relative content of Fe species (%) in Fe-NDC and $Yb_{0.4}$Fe-NDC.

at 85 °C is attributed to the removal of physically adsorbed solvent molecules. A second minor weight loss of 4.07% at 352 °C originates from the release of coordinated species, followed by a 15.2% weight loss at 391 °C associated with partial decomposition of the organic linker. A major weight loss of 24.74% occurs at 546 °C, corresponding to framework collapse and the formation of metal oxides. In comparison, pristine Fe-NDC exhibits three decomposition stages, including a 6.47% loss below 100 °C due to solvent removal, a 7.47% loss at 330 °C associated with coordinated species, and a major framework decomposition of 29.65% at 399 °C [47,48]. Notably, the primary decomposition temperature shifts to significantly higher values after Yb incorporation, indicating enhanced structural robustness and thermal stability, which are beneficial for long-term electrocatalytic durability. Zeta potential measurements were conducted to investigate the surface charge characteristics of the catalysts (Fig. 3c). All electrochemical measurements were performed in 1.0 M KOH aqueous electrolyte. Fe-NDC exhibits a zeta potential of −11.38 mV, indicating a moderately negatively charged surface with limited electrostatic repulsion that may promote particle aggregation. After Yb incorporation, the zeta potential of $Yb_{0.4}$Fe-NDC decreases substantially to −23.78 mV, indicating increased surface charge density and improved colloidal stability. This change is consistent with the successful incorporation of Yb into the framework, as confirmed by ICP-MS analysis (Table S1), which shows Yb content increasing systematically with increasing nominal feeding. This shift likely reflects modifications in surface functional groups and the electronic environment upon Yb incorporation. In alkaline electrolyte, the more negatively charged surface can enhance electrostatic interactions with hydroxide ions, thereby facilitating adsorption of OER-relevant intermediates and accelerating interfacial reaction kinetics [49–52]. X-ray photoelectron spectroscopy (XPS) was employed to probe the elemental composition and electronic states of the catalysts. The survey spectra (Fig. 3d) confirm the presence of C, O, Fe, and Yb, verifying successful incorporation of Yb into the Fe-NDC framework. The Fe 2p core-level spectra (Fig. 3e) were analyzed to investigate the oxidation states of Fe and the electronic influence of Yb doping. For pristine Fe-NDC, the Fe $2p_{3/2}$ region can be deconvoluted into Fe^{2+} and Fe^{3+} species located at 711.11 and 713.0 eV, respectively, together with a satellite peak at 717.11 eV [53]. In the Fe $2p_{1/2}$ region, Fe^{2+} and Fe^{3+} peaks appear at 724.17 and 725.78 eV, respectively, accompanied by a satellite peak at 727.81 eV. Following Yb incorporation, the Fe 2p peaks exhibit an overall positive shift of approximately 0.36 eV toward higher binding energy. This binding-energy shift reflects reduced core-hole screening at Fe sites, arising from electron withdrawal through the Fe-O-Yb network, which is consistent with the electron-withdrawal effect. Concurrently, the Fe^{3+}/Fe^{2+} ratio increases slightly, indicating that Yb doping also stabilizes Fe in a higher oxidation state through strengthened metal-ligand coordination. These observations collectively demonstrate that Yb^{3+} modulates the electronic environment of Fe centers via ligand-mediated electronic coupling, optimizing the adsorption energetics of oxygenated intermediates during OER. The O 1 s spectra (Fig. 3f) can be deconvoluted into three components. The peak centered at 529.82 eV corresponds to metal-oxygen (M-O) bonds, while the peak at 531.51 eV is assigned to carboxylate oxygen (O-C═O) from the NDC linker. The third peak at 532.88 eV originates from adsorbed water molecules [54,55]. After Yb doping, the intensities of all three peaks increase, suggesting enhanced surface oxygen content and improved hydrophilicity, which is consistent with the contact angle results and beneficial for OER performance. The C 1 s spectra (Fig. 3g) are deconvoluted into three components. The peak at 284.58 eV is assigned to C-C/C═C bonds from the aromatic rings of the NDC linker, the peak at 285.48 eV corresponds to C-O species, and the peak at 288.90 eV is attributed to carboxylate carbon (C═O) from the coordinated -COO groups [56]. The Yb 4d XPS spectrum (Fig. 3h) exhibits a characteristic multiplet structure associated with trivalent Yb^{3+}. The spectrum can be fitted into five peaks located at 186.23, 189.00, 193.98, 200.60, and 207.10 eV. Among these, the peaks at 186.23 and

193.98 eV correspond to the Yb $4d_{5/2}$ and Yb $4d_{3/2}$ spin-orbit components, respectively. The presence of a complex multiplet structure instead of a simple spin-orbit doublet confirms that Yb predominantly exists in the + 3-oxidation state within the Fe-NDC framework [57,58]. Importantly, no signals associated with Yb^{2+} species are detected at lower binding energies (~181–182 eV), indicating the absence of divalent Yb species. Quantitative analysis of the Fe 2p spectra (Fig. 3i) reveals that pristine Fe-NDC contains 17.48% Fe^{2+} and 55.48% Fe^{3+} species, whereas $Yb_{0.4}$Fe-NDC exhibits substantially altered Fe^{2+}/Fe^{3+} ratios of 14.12% and 53.7%, respectively. Together with the observed positive binding-energy shift, these results demonstrate that Yb incorporation significantly modulates the electronic structure and valence-state distribution of Fe centers, which is expected to play a critical role in optimizing OER catalytic activity. Multiple complementary characterizations confirm the uniform incorporation of Yb into the Fe-NDC crystal lattice. XRD shows preserved MOF crystallinity without segregated Yb-containing phases, while FTIR reveals no distinct Yb-O bands associated with Yb oxides or hydroxides. Systematic changes in wettability and zeta potential further support uniform lattice incorporation rather than random surface deposition of amorphous Yb species. Enhanced thermal stability from TGA indicates strengthened metal-ligand interactions upon Yb doping. ICP-MS confirms Yb retention close to the nominal composition, and EDS mapping shows a homogeneous distribution of Yb throughout the nanoplates. Additionally, the + 0.36-eV positive shift in Fe 2p binding energy indicates a direct electronic interaction between Yb and Fe centers.

3.2. Electrocatalytic OER performance

The OER performance of Fe-NDC, Yb_xFe-NDC (x = 0.2, 0.4, and 0.6), and RuO_2 was systematically evaluated in a three-electrode configuration using 1.0 M KOH electrolyte (Fig. 4a). As shown in Fig. 4b, $Yb_{0.4}$Fe-NDC exhibits exceptional electrocatalytic activity, requiring overpotentials of only 236, 255, and 271 mV to achieve current densities of 50, 100, and 200 mA cm^{-2}, respectively. These values are substantially lower than those of $Yb_{0.6}$Fe-NDC (241, 259, and 279 mV), $Yb_{0.2}$Fe-NDC (248, 267, and 291 mV), and pristine Fe-NDC (269, 288, and 309 mV) (Fig. 4c). Notably, $Yb_{0.4}$Fe-NDC also outperforms the noble-metal benchmark RuO_2, which requires overpotentials of 270 mV at 50 mA cm^{-2} and 319 mV at 200 mA cm^{-2}. Control experiments with bare NF (Fig. S4) confirm that the substrate contributes negligibly to the OER activity, ruling out any significant contribution from the NF support. Furthermore, independently prepared electrodes from different batches of $Yb_{0.4}$Fe-NDC show consistent performance, confirming reproducibility. The superior activity of $Yb_{0.4}$Fe-NDC demonstrates the critical role of optimized Yb incorporation in modulating the intrinsic catalytic properties of Fe-NDC. To gain further insight into the OER kinetics, Tafel slopes were extracted from the corresponding linear sweep voltammetry (LSV) curves (Fig. 4d). Among all catalysts, $Yb_{0.4}$Fe-NDC exhibits the smallest Tafel slope of 48 mV dec^{-1}, followed by $Yb_{0.6}$Fe-NDC (50 mV dec^{-1}), $Yb_{0.2}$Fe-NDC (60 mV dec^{-1}), and pristine Fe-NDC (72 mV dec^{-1}). In contrast, RuO_2 displays a significantly larger Tafel slope of 80 mV dec^{-1}. The markedly reduced Tafel slope of $Yb_{0.4}$Fe-NDC indicates substantially accelerated OER kinetics and more favorable reaction pathways after Yb incorporation. Fig. 4e further compares the Tafel slopes across different current-density regions, where $Yb_{0.4}$Fe-NDC

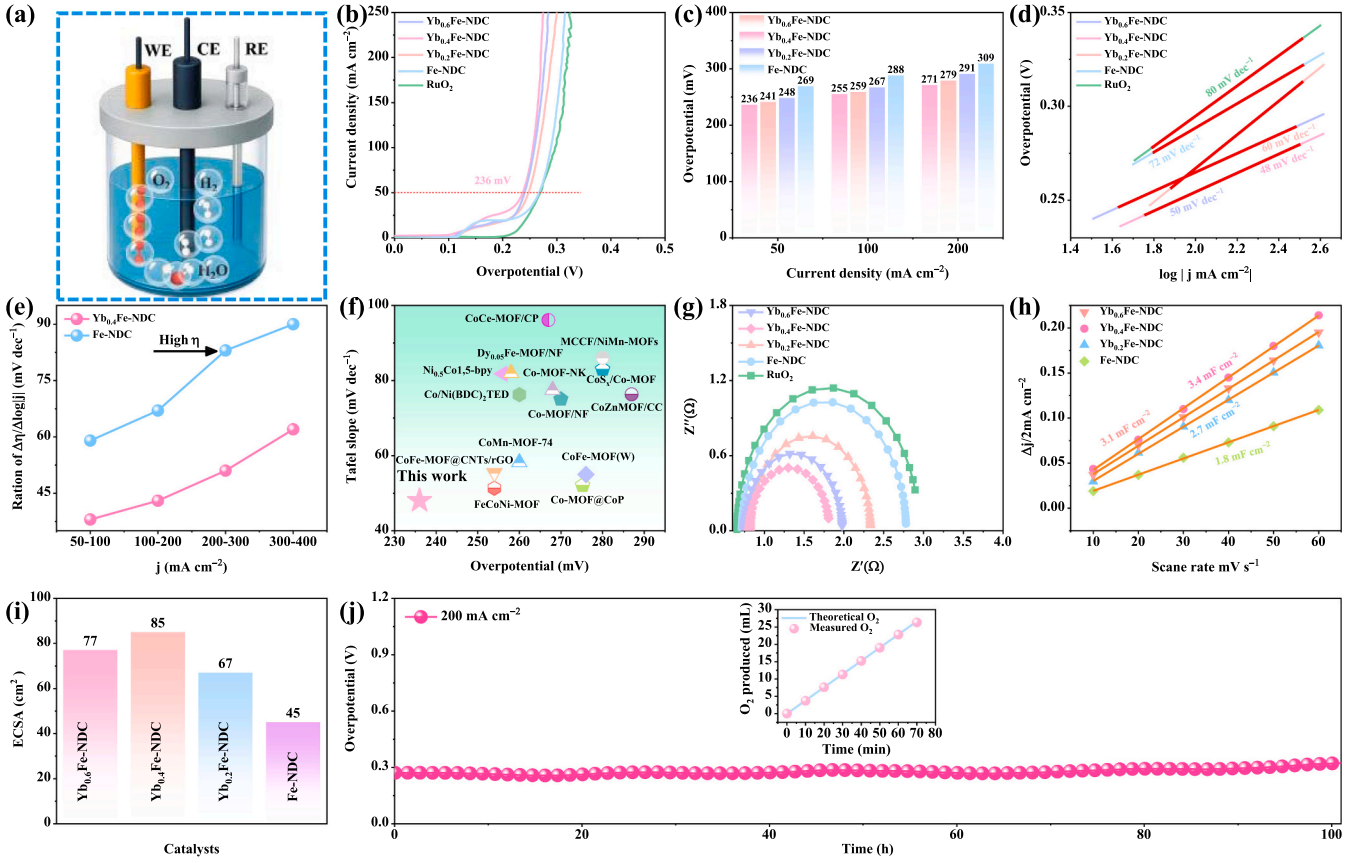

Fig. 4. OER electrocatalytic performance in 1.0 M KOH. (a) Schematic of the three-electrode system. (b) LSV curves of prepared electrocatalysts and RuO_2. (c) Overpotential comparison at different current densities. (d) Corresponding Tafel slopes of synthesized electrocatalysts. (e) Overpotential (η) ratio to log|j| at different current densities for Fe-NDC and $Yb_{0.4}$Fe-NDC. (f) Tafel slope and overpotential comparison with recently reported OER catalysts. (g) EIS, (h) C_{dl} plots and (i) corresponding ECSA values for all prepared catalysts. (j) Long-term CP stability test of $Yb_{0.4}$Fe-NDC at 200 mA cm^{-2} (inset, FE measurement for OER).

consistently maintains lower slope values than the other catalyst, suggesting that Yb doping effectively facilitates charge-transfer kinetics and optimizes the adsorption/desorption behavior of oxygen-containing intermediates during OER. The OER activity of $Yb_{0.4}$Fe-NDC compares favorably with, and in several cases surpasses, those of recently reported state-of-the-art electrocatalysts under alkaline conditions (Fig. 4 f and Table S1). Such enhanced catalytic performance can be attributed to the synergistic effects of ultrathin nanoplate morphology, increased active surface area, improved charge-transfer capability, and electronic modulation induced by Yb incorporation.

To further elucidate the origin of the enhanced catalytic activity, electrochemical impedance spectroscopy (EIS) measurements were conducted (Fig. 4 g). $Yb_{0.4}$Fe-NDC exhibits the smallest charge-transfer resistance (R_{ct} = 1.00 Ω) among all investigated catalysts, indicating significantly accelerated interfacial electron-transfer kinetics after Yb incorporation. In comparison, $Yb_{0.6}$Fe-NDC and $Yb_{0.2}$Fe-NDC show slightly higher R_{ct} values of 1.25 Ω and 1.56 Ω, respectively. Pristine Fe-NDC presents a markedly larger R_{ct} value of 2.08 Ω, reflecting slower charge-transfer kinetics. Notably, the R_{ct} of Fe-NDC remains lower than that of RuO_2 (2.26 Ω), highlighting the intrinsically favorable conductivity of the NDC-based framework. The corresponding equivalent circuit diagram used for EIS fitting, which complements the electrochemical analysis, is shown in Fig. S5. These results demonstrate that the improved OER activity originates from the synergistic interplay between Yb-induced electronic modulation and the optimized Fe-NDC framework. The electrochemically active surface area (ECSA) was subsequently evaluated by measuring the double-layer capacitance (C_{dl}) from cyclic voltammetry (CV) curves collected in the non-Faradaic region at different scan rates (Fig. S6). As shown in Fig. 4 h, $Yb_{0.4}$Fe-NDC exhibits a C_{dl} value of 3.4 mF cm^{-2}, which is substantially higher than that of pristine Fe-NDC (1.8 mF cm^{-2}). Correspondingly, the estimated ECSA values (Fig. 4i) are approximately 85 cm^2 for $Yb_{0.4}$Fe-NDC and 45 cm^2 for Fe-NDC, indicating that Yb incorporation effectively increases the number of electrochemically accessible active sites. The enlarged active surface area, together with improved electronic conductivity, contributes significantly to the enhanced OER performance. To exclude the influence of different mass loadings on the apparent catalytic activity, the LSV curves were normalized by ECSA to compare the intrinsic activity of the catalysts. As shown in Fig. S7a, the ECSA-normalized current density of $Yb_{0.4}$Fe-NDC is distinctly higher than those of the other prepared catalysts. Notably, at a fixed overpotential of 246 mV, $Yb_{0.4}$Fe-NDC also delivers the highest ECSA-normalized current (Fig. S7b), confirming its superior intrinsic OER activity. To further substantiate this, the mass-specific activities of all catalysts were calculated at the same overpotential (Fig. S8a). $Yb_{0.4}$Fe-NDC exhibits the highest mass activity of 17.07 A g^{-1}, significantly outperforming $Yb_{0.6}$Fe-NDC (13.55 A g^{-1}), $Yb_{0.2}$Fe-NDC (13.42 A g^{-1}), and Fe-NDC (8.37 A g^{-1}). Additionally, the turnover frequency (TOF) was calculated to assess the intrinsic catalytic efficiency, assuming all Fe sites (determined by ICP-MS) as the active centers. As shown in Fig. S8b, $Yb_{0.4}$Fe-NDC exhibits a significantly higher TOF than the other catalysts at the same potential, indicating superior intrinsic OER kinetics. Collectively, the ECSA-normalized, mass-specific, and TOF results consistently demonstrate that the enhanced OER performance of $Yb_{0.4}$Fe-NDC originates from Yb-induced electronic modulation rather than differences in catalyst loading. The Faradaic efficiency (FE) of $Yb_{0.4}$Fe-NDC was further evaluated by comparing the experimentally generated oxygen volume with the theoretical value (inset of Fig. 4j). The catalyst exhibits a FE close to 100%, confirming highly efficient conversion of electrical energy into oxygen evolution with negligible side reactions [9,59–62]. Long-term operational stability is another critical parameter for practical water-electrolysis applications. Therefore, the durability of $Yb_{0.4}$Fe-NDC was assessed by chronopotentiometry measurements at a high current density of 200 mA cm^{-2}. As shown in Fig. 4j, the catalyst maintains nearly constant operating potential over continuous operation for more than 100 h, demonstrating excellent electrochemical stability under strongly alkaline conditions. These results further highlight the robustness of the Yb-engineered Fe-NDC catalyst for long-term alkaline OER applications.

Compared with previously reported Fe-MOF-based OER catalysts, our $Yb_{0.4}$Fe-NDC presents several distinct advantages. First, the deliberate incorporation of Yb into the Fe-NDC framework introduces Fe-O-Yb bridging motifs that electronically modulate the Fe active sites a rare-earth doping strategy not yet explored in Fe-MOF systems for OER. Furthermore, the unique 2D nanoplate morphology maximizes active site exposure and facilitates rapid mass transport, enabling exceptional performance at high current densities (271 mV at 200 mA cm^{-2}). Most notably, the catalyst exhibits outstanding operational stability (>100 h at 200 mA cm^{-2}), which significantly exceeds the durability of most previously reported Fe-MOF electrocatalysts [63–67]. This superior stability is attributed to the strong oxophilic nature of Yb, which stabilizes the active phase and prevents structural degradation during prolonged electrolysis. These combined features Yb-induced electronic modulation, ultrathin 2D morphology, and exceptional durability distinguish our catalyst from prior Fe-MOF works and highlight the promise of rare-earth doping for high-current density water oxidation.

3.3. *Operando* and post-OER analysis

To investigate the interfacial charge-transfer behavior during OER, *operando* electrochemical impedance spectroscopy (EIS) measurements were conducted at various applied potentials. The corresponding Nyquist plots for Fe-NDC and $Yb_{0.4}$Fe-NDC are presented in Figs. S9a-b, respectively, while the associated Bode plots are shown in Fig. 5a ($Yb_{0.4}$Fe-NDC) and Fig. 5b (Fe-NDC). Across the entire investigated potential range, $Yb_{0.4}$Fe-NDC consistently exhibits lower charge-transfer resistance (R_{ct}) than pristine Fe-NDC, indicating substantially enhanced electronic conductivity and faster interfacial charge-transfer kinetics. Such improved charge-transfer behavior directly contributes to the superior electrocatalytic OER activity of the Yb-doped catalyst. The phase-angle evolution with applied potential is shown in Fig. 5c. For both catalysts, the phase angle gradually decreases with increasing potential, reflecting accelerated interfacial electrochemical processes during OER. Notably, the transition point appears at approximately 1.40 V for $Yb_{0.4}$Fe-NDC, whereas pristine Fe-NDC exhibits a delayed transition at around 1.45 V. The low-frequency region (0.1–100 Hz) is generally associated with charge-transfer processes at the catalyst/electrolyte interface during OER [68]. The earlier transition and lower impedance response observed for $Yb_{0.4}$Fe-NDC suggest more rapid electron-transfer kinetics and facilitated deprotonation of oxygenated intermediates compared with pristine Fe-NDC. These *operando* EIS results collectively demonstrate that Yb incorporation significantly accelerates interfacial charge-transfer dynamics, thereby promoting enhanced OER kinetics. To further elucidate the evolution of catalytically active species during OER, *operando* Raman spectroscopy was performed under applied potentials ranging from open-circuit potential (OCP) to 1.60 V. As shown in Fig. 5d, $Yb_{0.4}$Fe-NDC exhibits characteristic Raman bands in the 400–500 cm^{-1} region corresponding to FeOOH species beginning at an applied potential of approximately 1.30 V [69]. In contrast, similar FeOOH-related features appear for pristine Fe-NDC only at a higher potential of approximately 1.45 V (Fig. 5e). The earlier emergence of FeOOH species in $Yb_{0.4}$Fe-NDC indicates that Yb incorporation facilitates partial surface reconstruction of the catalyst surface into oxyhydroxide phases at lower applied potentials. This accelerated formation of FeOOH species, which correlates with the onset of enhanced OER activity, is a well-documented phenomenon in MOF-based electrocatalysts [70–72] and is likely a key factor contributing to the superior OER performance of the Yb-doped catalyst. Moreover, Raman spectra of bare NF were collected before and after CP at 200 mA cm^{-2} in 1.0 M KOH (Fig. S10). Pristine NF shows a featureless baseline, while after CP, two new peaks appear at 345 cm^{-1} (Ni-O) and 590 cm^{-1} (Ni-film), confirming substrate reconstruction [73]. In

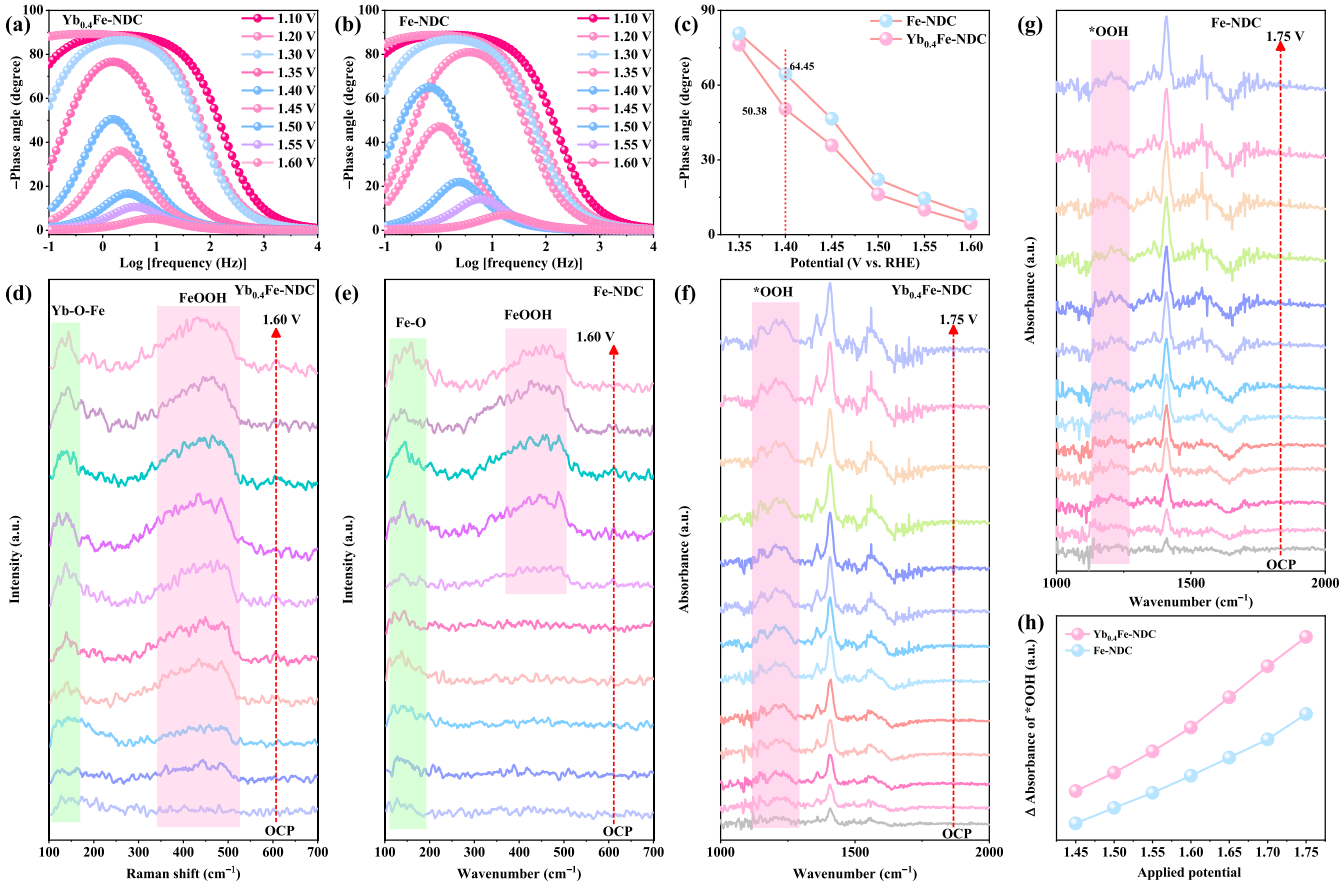

Fig. 5. *Operando* spectroscopic analysis. (a) *Operando* EIS bode plots of $Yb_{0.4}$Fe-NDC and (b) Fe-NDC at various applied potentials (vs. RHE). (c) Phase angle response of Fe-NDC and $Yb_{0.4}$Fe-NDC as function of applied potential. (d) *Operando* Raman spectra of $Yb_{0.4}$Fe-NDC and (e) Fe-NDC. (f) *Operando* ATR-FTIR spectra of $Yb_{0.4}$Fe-NDC and (g) Fe-NDC. (h) Integrated absorbance of the *OOH intermediate as a function of applied potential for Fe-NDC and $Yb_{0.4}$Fe-NDC.

contrast, the *operando* Raman spectra of Fe-NDC and $Yb_{0.4}$Fe-NDC exhibit Fe-derived oxyhydroxide peaks at distinctly different frequencies (400–500 cm^{-1}), confirming that the reconstructed active phase mainly originates from the catalyst.

To gain deeper mechanistic insight into the OER pathway, *operando* attenuated total reflectance Fourier-transform infrared (ATR-FTIR) spectroscopy was further conducted under applied potentials ranging from OCP to 1.75 V (Fig. 5f-g). At OCP, no obvious infrared absorption bands are observed for either catalyst. Upon increasing the applied potential, a distinct absorption peak gradually emerges at approximately 1207 cm^{-1}, which is assigned to the *OOH intermediate, a key reaction intermediate in the OER process [74,75]. The intensity of this *OOH--related peak continuously increases with increasing potential, indicating progressive accumulation of *OOH species during water oxidation. The integrated intensity of the *OOH peak as a function of applied potential is shown in Fig. 5h. Compared with pristine Fe-NDC, $Yb_{0.4}$Fe-NDC exhibits a significantly steeper increase and consistently higher *OOH intensity across the entire potential range, indicating more efficient formation and stabilization of the *OOH intermediate. These results suggest that Yb incorporation optimizes the adsorption energetics of oxygenated intermediates and accelerates the proton-coupled electron-transfer steps involved in OER. Importantly, the observation of *OOH intermediates rather than direct *OO species suggests that the OER proceeds through the conventional associative adsorbate evolution mechanism (AEM), involving four sequential proton-coupled electron-transfer steps, rather than through direct O-O coupling pathways [76]. To further distinguish between the AEM and the lattice oxygen mechanism (LOM), tetramethylammonium hydroxide (TMAOH) was employed as a chemical probe in combination with *operando* spectroscopic analysis. Peroxide-like (O_2^{2-}) and superoxide-like (O_2^{-}) species are generally considered representative intermediates of the LOM and AEM pathways, respectively. Because peroxide-like $*O_2^{2-}$ species are thermodynamically more stable and can strongly interact with TMA^+ ions, the addition of TMAOH can selectively suppress OER activity for catalysts operating through the LOM pathway [77,78]. The schematic illustration shown in the inset of Fig. 6a demonstrates this principle, where TMA^+ selectively complexes with peroxide-like intermediates, blocks active sites, and suppresses catalytic activity when the LOM pathway dominates. As shown in Fig. 6a, the LSV curves recorded in KOH electrolyte with and without TMA^+ exhibit negligible differences in OER activity. The absence of obvious activity suppression indicates that peroxide-like lattice oxygen intermediates are not involved in the reaction process. To further elucidate the oxygen evolution mechanism on the $Yb_{0.4}$Fe-NDC electrocatalyst, operando ^{18}O isotope-labeling differential electrochemical mass spectrometry (DEMS) was conducted. Fig. 6b displays the mass signals monitored at $m/z = 32$ ($^{16}O^{16}O$), 34 ($^{16}O^{18}O$), and 36 ($^{18}O^{18}O$) for the ^{18}O-labeled $Yb_{0.4}$Fe-NDC during OER in 1.0 M KOH prepared with $H_2^{16}O$. A strong signal corresponding to $m/z = 32$ is clearly observed, while the signals at $m/z = 34$ and 36 remain below the detection limit [79]. The absence of $^{16}O^{18}O$ and $^{18}O^{18}O$ species is consistent with an AEM, indicating that the evolved oxygen predominantly originates from the electrolyte water, with no detectable contribution from the catalyst lattice oxygen under the investigated conditions. The TMAOH chemical probe experiments and the ^{18}O isotope-labeling DEMS results provide complementary evidence that strongly supports the AEM pathway on $Yb_{0.4}$Fe-NDC. The absence of TMA^+-induced activity suppression rules out the involvement of peroxide-like ($*O_2^{2-}$) intermediates, while the dominant

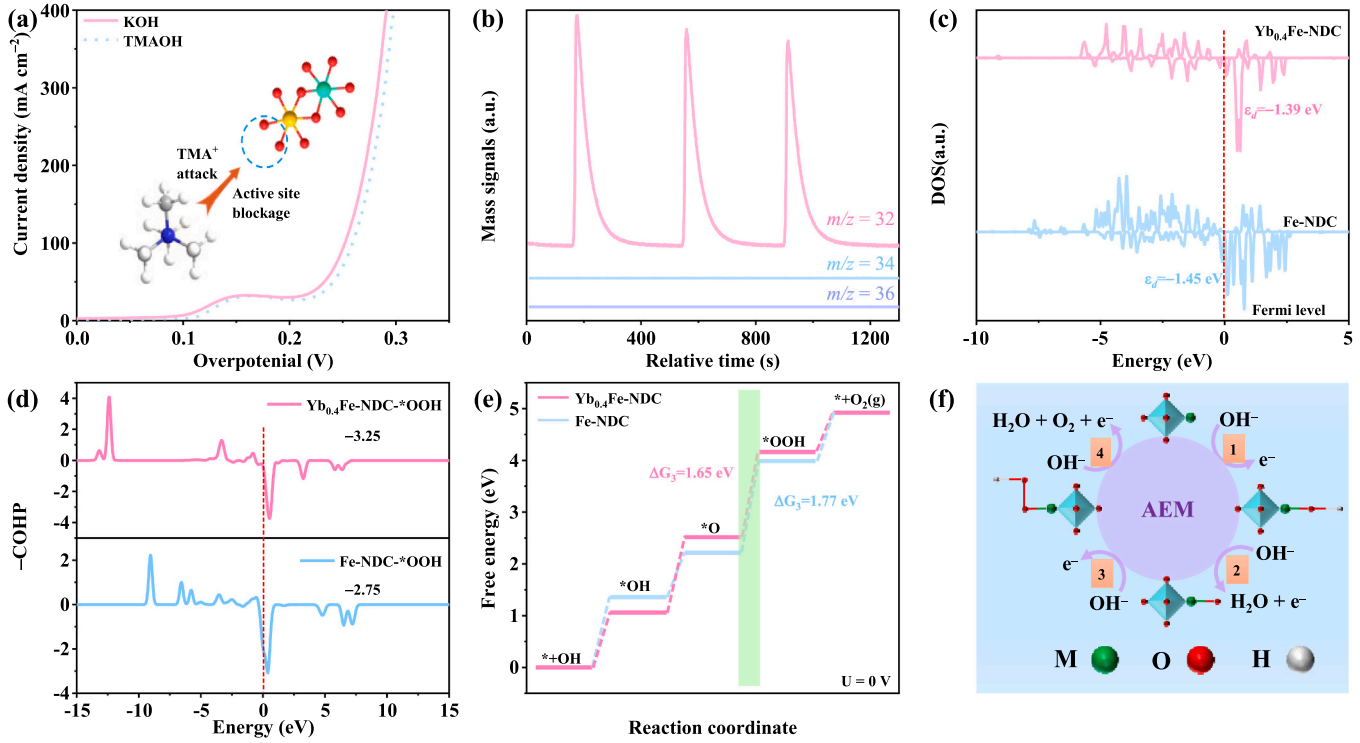

Fig. 6. (a) LSV curves of $Yb_{0.4}$Fe-NDC in 1.0 M KOH with and without TMA^+. The inset schematically illustrates that TMA^+ selectively blocks peroxide-like intermediates ($*O_2^{2-}$) under LOM, while having no effect on AEM. (b) DEMS analysis of gaseous products generated from the ^{18}O-labeled $Yb_{0.4}$Fe-NDC catalyst during OER in 1.0 M KOH ($H_2^{16}O$). DFT calculations of Fe-NDC and Yb doped Fe-NDC. (c) DOS of Fe-NDC and $Yb_{0.4}$Fe-NDC. (d) COHP of Fe-NDC-*OOH bond for $Yb_{0.4}$Fe-NDC-*OOH. (e) Gibbs free-energy diagrams of Fe-NDC and $Yb_{0.4}$Fe-NDC for OER under an applied potential of 0 V. (f) Schematic illustration of the adsorbate evolution mechanism (AEM) for the OER on the Fe active site, proceeding via four sequential proton-coupled electron transfer steps.

detection of $^{32}O_2$ is consistent with the evolved oxygen originating primarily from the electrolyte water. Collectively, these findings strongly support that the OER on $Yb_{0.4}$Fe-NDC proceeds predominantly via the conventional AEM rather than the LOM. This mechanistic assignment is further corroborated by the *operando* ATR-FTIR results, which reveal the formation of *OOH intermediates during the OER process.

To assess the structural and chemical stability following prolonged OER operation, comprehensive post-catalysis characterization was conducted on $Yb_{0.4}$Fe-NDC following the CP test. The SEM images (Fig. S11) reveal that the original 2D nanoplate morphology is largely retained, though slight surface roughening and minor structural densification are observed, consistent with structural evolution during prolonged electrochemical operation. TEM (Fig. S12a) further confirms the retention of the ultrathin nanoplate architecture, indicating that the nanoscale thickness and high active surface area are maintained during extended electrolysis. HR-TEM analysis (Fig. S12b) shows no distinct lattice fringes, consistent with above HR-TEM results. HAADF-STEM (Fig. S12c) demonstrates uniform elemental distribution within the nanoplate. Importantly, the corresponding elemental mapping (Figs. S12d-g) and the post-reaction EDS spectrum (Fig. S12h) confirm the homogeneous distribution of C, O, Fe, and Yb, with no detectable loss or aggregation of the metal species. To quantitatively evaluate elemental stability, ICP-MS was performed on both the recovered catalyst and the post-reaction electrolyte (Table S2). The results show a slight decrease in Fe content and a much more pronounced depletion of Yb, with the dissolved metal ions quantitatively recovered in the electrolyte. This preferential leaching of Yb suggests that the Yb-O coordination bonds are less stable under anodic alkaline conditions, leading to its gradual dissolution from the framework. Notably, despite this partial loss of Yb from the bulk, the post-reaction SEM and TEM data confirm that the overall 2D nanoplate architecture remains uncompromised, underscoring that the Fe-NDC backbone acts as the primary structural scaffold. Furthermore, EDS mapping confirms that the remaining Yb, along with Fe, is still uniformly distributed throughout the structure. This combination of structural preservation and homogeneous elemental dispersion rationalizes the sustained catalytic activity and excellent durability observed during the long-term high-current-density test. Beyond bulk composition and morphology, the evolution of surface chemical states was investigated via post-reaction XPS (Fig. S13). The O 1 s spectrum (Fig. S14a) shows a slight decrease in the intensities of all three components (M-O, O-C═O, and H_2O_{ads}) after prolonged operation, indicating partial loss of surface oxygen species and organic linkers. In the Fe 2p spectrum (Fig. S14b), a small negative shift (toward lower binding energy) is observed compared to the fresh catalyst, suggesting further oxidation of Fe species and the formation of active (oxy) hydroxide phases [80]. Importantly, the Yb 4d spectrum (Fig. S14c) retains the characteristic multiplet structure of Yb^{3+}, with peaks corresponding to an oxide-like coordination environment. This observation unambiguously confirms that Yb maintains its + 3-oxidation state and remains stably anchored within the partially reconstructed surface layer, contrasting with the dynamic changes observed for Fe. Collectively, these post-catalysis analyses establish that $Yb_{0.4}$Fe-NDC undergoes a favorable partial surface reconstruction into an active (oxy) hydroxide phase, while its 2D morphology and the trivalent state of Yb are effectively preserved. The ICP-MS results show that approximately 61% of the initial Yb remains incorporated after prolonged OER operation, indicating that Yb is not merely a sacrificial promoter but continues to play a structural role within the reconstructed surface layer. This retained Yb, confirmed by post-catalysis XPS to remain in the + 3-oxidation state, likely contributes to the electronic stabilization of the FeOOH-rich active phase. Meanwhile, the partial leaching of Yb (~39%) suggests that a fraction of Yb initially accelerates the surface reconstruction process, promoting the formation of the catalytically active oxyhydroxide species at lower potentials. Thus, Yb serves a dual function: it acts as a promoter that facilitates early reconstruction into

the active FeOOH phase, while the fraction that remains integrated into the reconstructed layer contributes to long-term structural and electronic stability. This synergy between beneficial surface transformation and structural robustness underpins the outstanding long-term durability of $Yb_{0.4}$Fe-NDC.

3.4. DFT calculations

Density functional theory (DFT) calculations were performed on the optimized structures of Fe-NDC and $Yb_{0.4}$Fe-NDC to elucidate the electronic modulation induced by Yb incorporation (Figs. S15a-b). The total density of states (DOS) analysis reveals that Yb doping shifts the D-band center of the Fe active sites upward from −1.45 eV in pristine Fe-NDC to −1.39 eV in $Yb_{0.4}$Fe-NDC (Fig. 6c) [81]. According to D-band center theory, an upward shift of the D-band center toward the Fermi level strengthens the interaction between the catalyst surface and oxygen-containing intermediates by reducing the occupation of antibonding states formed between Fe d orbitals and adsorbate orbitals [82]. Consequently, the adsorption energetics of key OER intermediates, including *OH, *O, and *OOH, become more favorable. In addition, the projected density of states (PDOS) analysis demonstrates significantly enhanced orbital hybridization between Fe 3d and O 2p states near the Fermi level in $Yb_{0.4}$Fe-NDC compared with pristine Fe-NDC (Fig. S16). The strengthened Fe 3d-O 2p hybridization indicates increased metal-oxygen covalency, which can facilitate interfacial electron transfer and optimize the binding strength of oxygenated intermediates during OER.

To further investigate the interaction between the active sites and the key *OOH intermediate, crystal orbital Hamilton population (COHP) analysis was conducted for the Fe-*OOH bond (Fig. 6d). The integrated COHP (ICOHP) value for $Yb_{0.4}$Fe-NDC is calculated to be −3.25 eV, which is substantially more negative than the value of −2.75 eV obtained for pristine Fe-NDC. This result confirms a significantly stronger bonding interaction between the Fe active centers and *OOH after Yb incorporation, consistent with the upward shift of the Fe D-band center [83]. The stronger Fe-*OOH interaction facilitates stabilization of the key reaction intermediate and promotes subsequent proton-coupled electron-transfer processes during OER. This enhanced interaction is reconciled with the XPS observation of a + 0.36 eV positive shift in Fe 2p binding energy, which together with DFT reveals that electron withdrawal from Fe coexists with an upshifted D-band center. This combination is explained by electronic modulation through the Fe-O-Yb bridging motif. The highly Lewis acidic Yb polarizes the bridging oxygen, strengthening the Yb-O interaction and altering the Fe 3d-O 2p hybridization. This ligand-field modification raises the Fe D-band energy despite net electron depletion at Fe, consistent with electronic effects reported for rare-earth-doped transition metal oxides and MOFs [84–87]. Consequently, the upshifted D-band center strengthens Fe-*OOH interactions and facilitates oxygen intermediate adsorption. The Gibbs free-energy profiles for OER following the AEM pathway are presented in Fig. 6e. Both catalysts follow a conventional four-electron AEM pathway, in which the transformation from *O to *OOH is identified as the potential-determining step. Notably, Yb incorporation substantially reduces the free-energy barrier (ΔG_3) of this step from 1.77 eV for pristine Fe-NDC to 1.65 eV for $Yb_{0.4}$Fe-NDC [88]. This reduction indicates that Yb doping significantly facilitates the formation of the *OOH intermediate, thereby accelerating overall OER kinetics. The optimized adsorption configurations of all OER intermediates on Fe-NDC and $Yb_{0.4}$Fe-NDC are presented in Figs. S17-S18. The coordination structures show that the intermediates bind to the Fe site via oxygen, with Yb doping inducing subtle structural changes that optimize intermediate adsorption and lower the *OOH formation barrier. The detailed AEM pathway in alkaline electrolyte is schematically illustrated in Fig. 6f. The OER proceeds through four sequential proton-coupled electron-transfer steps occurring on the catalyst surface. Initially, hydroxide ions (OH^-) adsorb onto the active sites to form *OH intermediates (ΔG_1). Subsequent deprotonation generates *O species (ΔG_2), followed by nucleophilic attack of another OH^- ion to form the *OOH intermediate (ΔG_3). Finally, the *OOH intermediate undergoes deprotonation and O-O bond cleavage to release O_2 and regenerate the active site (ΔG_4) [89]. The proposed AEM pathway is strongly supported by *operando* Raman and ATR-FTIR results, which directly identify the formation of *OOH intermediates during OER. Moreover, TMA^+ probe experiments exhibit negligible suppression of catalytic activity, ruling out significant LOM participation, while DEMS analysis confirms that the evolved O_2 ($m/z = 32$) originates from water oxidation via the AEM pathway. Collectively, the DFT calculations and *operando* spectroscopic results demonstrate that Yb incorporation modulates the electronic structure of Fe active centers through upward shifting of the d-band center, enhanced Fe 3d-O 2p hybridization, and strengthened *OOH adsorption. These electronic effects, together with the accelerated surface reconstruction, improved kinetics, and structural advantages of the 2D morphology, synergistically optimize the adsorption energetics of oxygen intermediates and accelerate OER kinetics via the AEM pathway. This multifaceted synergy ultimately accounts for the superior electrocatalytic performance of $Yb_{0.4}$Fe-NDC.

3.5. Performance in water electrolyzers device

The development of highly efficient and durable electrocatalysts is essential for advancing overall water splitting and sustainable hydrogen production. To evaluate the practical applicability of $Yb_{0.4}$Fe-NDC, a two-electrode alkaline water-electrolysis system was assembled using $Yb_{0.4}$Fe-NDC supported on NF as the OER anode and commercial Pt/C on NF as the HER cathode. The schematic illustration in Fig. 7a depicts the overall water-splitting process and highlights the potential utilization of the generated green hydrogen in various applications, including hydrogen refueling stations, chemical manufacturing, fuel cells, gas turbines, residential heating, industrial processes, and maritime transportation. This demonstration highlights the practical relevance of the $Yb_{0.4}Fe\text{-}NDC^{(+)}||^{(-)}Pt/C$ electrolyzer toward the development of a sustainable hydrogen economy.

The overall water-splitting performance of the $Yb_{0.4}Fe\text{-}NDC^{(+)}||^{(-)}Pt/C$ system was evaluated in 1.0 M KOH and benchmarked against the $RuO_2^{(+)}||^{(-)}Pt/C$ electrolyzer (Fig. S19). As shown in Fig. 7b, the $Yb_{0.4}$Fe-NDC-based electrolyzer requires a cell voltage of only 1.46 V to achieve a current density of 50 mA cm^{-2}, which is lower than the 1.49 V required for the RuO_2-based system. More importantly, under high-current-density conditions, the performance advantage of $Yb_{0.4}$Fe-NDC becomes increasingly pronounced. At current densities of 200 and 400 mA cm^{-2}, the $Yb_{0.4}Fe\text{-}NDC^{(+)}||^{(-)}Pt/C$ system requires cell voltages of only 1.57 and 1.64 V, respectively, whereas the $RuO_2^{(+)}||^{(-)}Pt/C$ electrolyzer requires significantly higher voltages of 1.63 and 1.73 V (Fig. 7c). These values compare favorably with those of recently reported MOF-based water-splitting electrocatalysts, highlighting the outstanding performance of the Yb-engineered Fe-NDC system (Fig. 7d and Table S4). Long-term durability under continuous operating conditions is another critical requirement for practical water electrolysis. Therefore, the operational stability of the $Yb_{0.4}Fe\text{-}NDC^{(+)}||^{(-)}Pt/C$ electrolyzer was systematically evaluated under continuous high-current-density electrolysis. At a current density of 200 mA cm^{-2}, the system maintains stable operation for over 160 h without obvious performance degradation (Fig. S20a). Even under the more demanding condition of 400 mA cm^{-2}, the electrolyzer remains highly stable for 128 h (Fig. S20b). The excellent durability demonstrates that the Yb-doped Fe-NDC anode can effectively with stand prolonged exposure to harsh alkaline OER conditions while maintaining high catalytic activity.

To further assess the practical feasibility of the as-prepared electrocatalyst, the $Yb_{0.4}$Fe-NDC is directly served as the anode and commercial Pt/C as the cathode ($Yb_{0.4}Fe\text{-}NDC^{(+)}||^{(-)}Pt/C$) for assembling the AEMWE (Fig. 7e). The electrolyzer was investigated at different

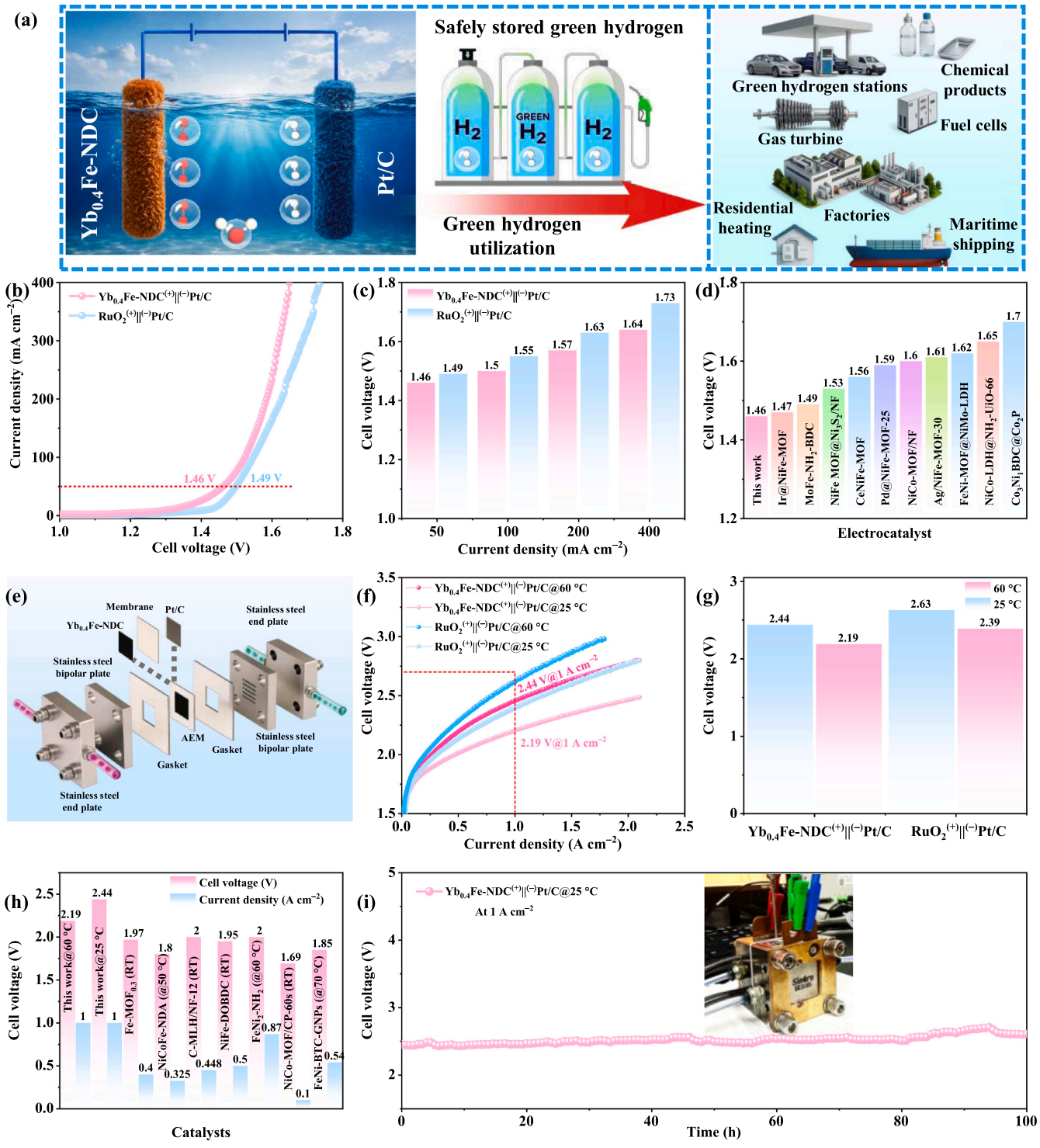

Fig. 7. (a) Schematic illustration of the two-electrode system for water electrolysis and green hydrogen utilization. (b) LSV curves of $Yb_{0.4}Fe\text{-}NDC^{(+)}||^{(-)}Pt/C$ and $RuO_2^{(+)}||^{(-)}Pt/C$ for water electrolysis. (c) Cell voltage comparison at different current densities (50, 100, 200 and 400 mA cm^{-2}). (d) Comparison with recently reported MOF-based electrocatalysts. (e) Schematic illustration of the anion exchange membrane water electrolyzer (AEMWE) configuration. (f) Polarization (LSV) curves of the AEMWE recorded in 1.0 M KOH at 25 and 60 °C. (g) Comparison of the AEMWE cell voltages measured at 25 and 60 °C. (h) Benchmark comparison of the AEMWE performance with recently reported MOFs-based electrocatalysts. (i) CP stability test of the $Yb_{0.4}Fe\text{-}NDC^{(+)}||^{(-)}Pt/C$ electrolyzer operated at a constant current density of 1 A cm^{-2} under ambient conditions.

temperatures in a 1.0 M KOH electrolyte; enhanced performance was observed when the operating temperature increased from 25 °C to 60 °C. Notably, a cell voltage of 2.44 V achieves a current density of 1.0 A cm^{-2} at 25 °C, and this is further reduced to 2.19 V at 1.0 A cm^{-2} when the temperature is increased to 60 °C (Fig. 7f). The improved performance at elevated temperature arises from accelerated reaction kinetics and enhanced ionic conductivity. For comparison, a benchmark $RuO_2^{(+)}||^{(-)}Pt/C$ electrolyzer requires 2.63 V at 25 °C and 2.39 V at 60 °C to achieve 1.0 A cm^{-2}, underscoring the superior activity of $Yb_{0.4}Fe\text{-}NDC$ (Fig. 7g). This performance surpasses many previously reported MOF-based AEMWE systems under comparable conditions (Fig. 7h and Table S5). The AEMWE exhibits excellent stability, with negligible

voltage increase over 100 h of continuous operation at 1.0 A cm^{-2} at room temperature (Fig. 7i), confirming the robust durability of the $Yb_{0.4}$Fe-NDC anode at ampere-level current densities.

3.6. Origin of the superior OER performance

The superior OER performance of $Yb_{0.4}$Fe-NDC originates from a synergistic combination of structural, electronic, mechanistic, and computational factors. (i) Morphologically, the ultrathin 2D nanoplates architecture maximizes active site exposure and facilitates rapid mass transport and gas bubble detachment, essential for high-current-density operation. (ii) Electronically, the incorporation of Yb^{3+} shifts the Fe 2p binding energy to higher values, modulating the electronic environment of iron centers to optimize the adsorption energy of oxygenated intermediates, an effect supported by DFT calculations, which reveal that Yb doping upshifts the Fe d-band center from −1.45 eV to −1.39 eV, strengthens the Fe-*OOH bond (-ICOHP from 2.75 eV to 3.25 eV), and lowers the *OOH formation barrier from 1.77 eV to 1.65 eV. (iii) *Operando* Raman spectroscopy shows that the active FeOOH phase emerges at a lower potential (1.30 V for $Yb_{0.4}$Fe-NDC vs. 1.45 V for Fe-NDC), enabling earlier formation of catalytically competent sites. (iv) Mechanistically, *operando* ATR-FTIR, TMA^+ probing and DEMS confirm that the reaction follows the AEM with *OOH as the key intermediate, excluding the lattice oxygen pathway and ensure stability. (v) Kinetic efficiency is reflected in a low Tafel slope of 48 mV dec^{-1} and significantly reduced charge transfer resistance, indicating faster electron transfer at the catalyst-electrolyte interface. (vi) Finally, practical robustness is demonstrated by stable operation exceeding 100 h at 200 mA cm^{-2} and a two-electrode system ($Yb_{0.4}Fe\text{-}NDC^{(+)}||^{(-)}Pt/C$) that delivers 1.64 V at 400 mA cm^{-2} with over 128 h of durability. Moreover, in AEMWE, the catalyst achieves cell voltages of 2.44 V at 25 °C and 2.19 V at 60 °C at 1.0 A cm^{-2}, with stable operation exceeding 100 h, highlighting its practical potential for high-current-density electrolysis. Collectively, these findings demonstrate that rare-earth doping plays a crucial role in simultaneously optimizing the structural and electronic properties of MOF-based catalysts for practically relevant water oxidation.

4. Conclusion

In summary, we have developed a 2D Yb-doped Fe-NDC electrocatalyst via a one-step solvothermal strategy for efficient alkaline OER and overall water splitting. Benefiting from the ultrathin nanoplate morphology and Yb-induced electronic modulation, the optimized $Yb_{0.4}$Fe-NDC exhibits a low overpotential of 271 mV at 200 mA cm^{-2} and a small Tafel slope of 48 mV dec^{-1}, with stable operation exceeding 100 h. *Operando* spectroscopy confirms the adsorbate evolution mechanism via *OOH intermediates, and DFT calculations reveal that Yb upshifts the Fe d-band center, strengthens Fe-OOH interaction, and lowers the *OOH formation barrier. In a two-electrode electrolyzer, the $Yb_{0.4}Fe\text{-}NDC^{(+)}||^{(-)}Pt/C$ system achieves cell voltages of 1.57 V at 200 mA cm^{-2} and 1.64 V at 400 mA cm^{-2}, with durable operation for 160 and 128 h, respectively. Furthermore, in AEMWE, it delivers a cell voltage of 2.44 V at 1.0 A cm^{-2} at 25 °C and 2.19 V at 60 °C, with stable operation for over 100 h, demonstrating its practical potential for high-current-density water electrolysis. This work establishes rare-earth electronic modulation as an effective strategy for designing high-performance MOF electrocatalysts for high-current-density water splitting.

CRediT authorship contribution statement

Sheraz Muhammad: Writing – original draft, Methodology, Investigation, Formal analysis, Data curation. **Sumayya Khan**: Data curation. **Sana Zahoor**: Investigation. **Rahmat Ullah**: Conceptualization. **Ali Aman**: Formal analysis. **Tayirjan Taylor Isimjan**: Writing – review & editing. **Shohreh Azizi**: Writing – review & editing. **Xiulin Yang**: Writing – review & editing, Supervision, Resources, Project administration, Funding acquisition, Conceptualization.

Declaration of Competing Interest

The authors declare that they have no known competing financial interests or personal relationships that could have appeared to influence the work reported in this paper.

Acknowledgements

This work was financially supported by the Guangxi Science and Technology Projects (GUIKE LT2600640010), the Natural Science Foundation of Guangxi Province (2026GXNSFBA00640178), and the National Natural Science Foundation of China (52363028; W2621022; 21965005). I, Sheraz Muhammad, a PhD student at Guangxi Normal University, am also deeply grateful to the China Scholarship Council (CSC) for providing the scholarship that supports my doctoral studies in China.

Appendix A. Supporting information

Supplementary data associated with this article can be found in the online version at doi:10.1016/j.apcatb.2026.127265.

References

[1] Z. Wang, M. Liu, Z. Tan, Y. Wang, Y. Liang, B. Liang, Y. Hu, Y. Yang, C. Duan, K. Qi, H. Xi, MOF-based catalysts for oxygen evolution reaction: Evaluation criteria and catalytic performance insights, Nano Mater. Sci. 8 (742) (2026), https://doi.org/10.1016/j.nanoms.2025.12.010.

[2] W. Zhou, Y. Huang, H. Cai, T. Wang, H. Li, C. Zhang, L. Zhao, L. Chen, M. Liao, Z. Tang, K. Chen, J. Gu, W. Gao, Z. Fan, Z. Wen, A Strongly Coupled Cluster Heterostructure with Pt–N-Mo Bonding for Durable and Efficient H_2 Evolution in Anion-Exchange Membrane Water Electrolyzers, Nano-Micro Lett. 17 (2025) 296, https://doi.org/10.1007/s40820-025-01798-x.

[3] P. Yang, C. Yang, Z. Wu, Z. Tang, Evolving metal-organic frameworks for highly active oxygen evolution, Matter 8 (2025) 102046, https://doi.org/10.1016/j.matt.2025.102046.

[4] L. Chen, Y. Huang, H. Li, R. Gao, H. Tang, J. Chen, Y. Wang, M. Liao, C. Wu, Polyoxometalate-derived N@Mo_2C/V_2O_3 cluster heterostructure for accelerated alkaline hydrogen evolution reaction, Polyoxometalates 5 (2026) 9140110, https://doi.org/10.26599/POM.2026.9140110.

[5] Z. Huang, B. Wu, S. Zhang, C. Xu, Y. Hu, L. Wang, B. Liu, B. Fu, X. Shi, M. Gao, A. Zhou, X. Yang, T. Zhang, L. Jiao, Spin-State Engineering of Ni Centers by Dual-Ligand Competitive Coordination for Superior Oxygen Evolution Reaction, Angew. Chem. Int. Ed. 65 (2026) e9878440, https://doi.org/10.1002/anie.9878440.

[6] W. Zhang, Y. Xiao, L. Li, Z. Yu, J. Feng, C. Zhong, W.F. Ip, H. Pan, Dynamic Mo leaching and vacancy engineering synergize HER and OER kinetics in NiFe-based catalysts for overall water electrolysis, Mater. Horiz. 12 (2025) 10901–10910, https://doi.org/10.1039/D5MH01366F.

[7] Y. Chen, M. Tian, Z. Zhang, G. Wang, Y. Guo, J. Wu, D. Qi, Z. Yan, X. Liu, X. Liu, Deliberate design of MOF-based pre-catalyst rationalizing the structural reconstruction toward efficient oxygen evolution reaction, Sci. China Chem. 68 (2025) 2388–2398, https://doi.org/10.1007/s11426-024-2453-2.

[8] J. Jia, Y. Wang, Y. Cha, Z. Wang, J. Huang, D. Wang, H. Li, K. Guo, J. Li, J. Huang, Boosting OER performance of NiFe-MOFs via heterostructure engineering: promoted phase transformation and self-optimized dynamic interface electron structure, Adv. Funct. Mater. 35 (2025) 2500568, https://doi.org/10.1002/adfm.202500568.

[9] K. Yue, J. Liu, C. Xia, K. Zhan, P. Wang, X. Wang, Y. Yan, B.Y. Xia, Controllable synthesis of multidimensional carboxylic acid-based NiFe MOFs as efficient electrocatalysts for oxygen evolution, Mater. Chem. Front. 5 (2021) 7191–7198, https://doi.org/10.1039/D1QM00960E.

[10] D.H. Taffa, D. Balkenhohl, M. Amiri, M. Wark, Minireview: Ni–Fe and Ni–Co metal–organic frameworks for electrocatalytic water-splitting reactions, Small Struct. 4 (2023) 2200263, https://doi.org/10.1002/sstr.202200263.

[11] C. Ding, W. Zhong, Y. Cao, T. Ma, H. Ye, Z. Fang, Y. Feng, S. Zhao, J. Yang, Y. Li, L. Shen, W. He, Fe-MOF-based catalysts for oxygen evolution reaction: Microenvironment regulated by organic ligands, metals and carbonization synergistically, Chem. Eng. Sci. 302 (2025) 120888, https://doi.org/10.1016/j.ces.2024.120888.

[12] X. Zhang, W. Jiang, J. Di, Rational Design and Application of MOF-Based Materials for Photocatalytic CO_2 Reduction, Small 22 (2026) e13278, https://doi.org/10.1002/smll.202513278.

[13] G. Yilmaz, S.B. Peh, D. Zhao, G.W. Ho, Atomic-and molecular-level design of functional metal–organic frameworks (MOFs) and derivatives for energy and environmental applications, Adv. Sci. 6 (2019) 1901129, https://doi.org/10.1002/advs.201901129.
[14] H. Yin, Z. Lin, L. Wang, Y. Huang, T.T. Isimjan, X. Yang, Leveraging ligand push-pull effects in Ni-based MOFs for optimized lattice oxygen activation and superior water oxidation, Appl. Catal. B Environ. Energy 378 (2025) 125610, https://doi.org/10.1016/j.apcatb.2025.125610.
[15] Z. Huang, D. Eder, Harnessing the structural evolution of metal–organic frameworks under electrocatalytic conditions, Commun. Chem. 8 (2025) 359, https://doi.org/10.1038/s42004-025-01747-0.
[16] A.H. Mamaghani, J. Liu, Z. Zhang, R. Gao, Y. Wu, H. Li, M. Feng, Z. Chen, Promises of MOF-Based and MOF-Derived Materials for Electrocatalytic CO_2 Reduction, Adv. Energy Mater. 14 (2024) 2402278, https://doi.org/10.1002/aenm.202402278.
[17] S. Muhammad, H. Sun, S. Zahoor, S. Khan, R. Ullah, B. Fu, S. Ullah, T.T. Isimjan, S. Azizi, X. Yang, Advancing MOFs for electrocatalytic ORR, UOR, and CO_2RR: From fundamentals to device integration and deployment challenges, Mater. Sci. Eng. R. Rep. 171 (2026) 101248, https://doi.org/10.1016/j.mser.2026.101248.
[18] Z. Xu, Y. Tao, Z. Sun, P. Bi, X. Zhong, J. Liao, D. Hao, L. Yang, L. Xu, M. Luo, K. Pan, Z. Gao, Ligand-engineered Ni-based metal–organic frameworks for electrochemical oxygen evolution reaction, Chem. Eng. J. 478 (2023) 147418, https://doi.org/10.1016/j.cej.2023.147418.
[19] S. Li, W. Liu, Y. Shi, T. Wang, T. Liu, X. Xue, R. Li, M. Qiao, Z.-Y. Wu, W. Zhang, Ligand-rich oxygen evolution electrocatalysts reconstructed from metal-organic frameworks for anion-exchange membrane water electrolysis, Sci. Bull. 70 (2025) 1976–1985, https://doi.org/10.1016/j.scib.2025.04.037.
[20] R. Ren, J. Wang, Y. Xie, T. Li, H. Wei, F. Wang, H. Yang, Z. Lin, J. Gao, Fe-doping accelerates the reconstruction kinetics of metal-organic frameworks toward active amorphous oxyhydroxide enabling industrial water splitting, Appl. Catal. B Environ. Energy 388 (2026) 126543, https://doi.org/10.1016/j.apcatb.2026.126543.
[21] D. Shen, W. Ke, G. Balati, Y. Li, Tungsten doping-Induced electronic structure modulation in NiFe-based metal-organic frameworks for enhanced oxygen evolution reaction, Int. J. Hydrog. Energy 69 (2024) 215–222, https://doi.org/10.1016/j.ijhydene.2024.04.355.
[22] T. Zhao, D. Zhong, Q. Fang, D. Li, G. Hao, G. Liu, J. Li, Q. Zhao, Shifting the Oxygen-Evolution Reaction Pathway via Cation Engineering to Activate Lattice Oxygen in Metal–Organic Frameworks, ACS Appl. Mater. Interfaces 16 (2024) 27291–27300, https://doi.org/10.1021/acsami.4c01872.
[23] S. Muhammad, L. Wang, M. Gao, S. Khan, W. Xu, A. Ali, T.T. Isimjan, S. Azizi, X. Yang, Fe-Ce interaction-driven active site modulation in a porous MOF for oxygen evolution reaction, Fuel 405 (2026) 136782, https://doi.org/10.1016/j.fuel.2025.136782.
[24] H. Yin, M. Huang, L. Wang, S. Muhammad, T.T. Isimjan, J. Guo, D. Cai, B. Wang, X. Yang, Lattice-mismatched MOF-on-MOF nanosheets with rich oxygen vacancies show fast oxygen evolution kinetics for large-current water splitting, Appl. Catal. B Environ. Energy 367 (2025) 125105, https://doi.org/10.1016/j.apcatb.2025.125105.
[25] M. Etesami, S.R. Motlagh, R. Khezri, M. Gopalakrishnan, J. Theerthagiri, M. Y. Choi, K. Nootong, A. Somwangthanaroj, S. Kheawhom, MOF-derived LDHs: Unveiling their potential in oxygen evolution reaction, EnergyChem 6 (2024) 100128, https://doi.org/10.1016/j.enchem.2024.100128.
[26] S. Khamsanga, S. Kheawhom, P. kidkhunthod, W. Limphirat, J. Qin, D. kido, X. Zhao, P. Pattananuwat, Metalloporphyrin MOF-derived Ni-doped CO_3O_4 embedded CeO_2-Co_3O_4 heterostructures as highly efficient and durable bifunctional ORR/OER catalysts for zinc-air batteries, Chem. Eng. J. Adv. 26 (2026) 101178, https://doi.org/10.1016/j.ceja.2026.101178.
[27] Y. Song, Y. Li, Q. Qi, C. Zhang, J. Hu, Controlled Reconstruction of MOF via Enhanced C—O Bonding for Oxygen Evolution, Adv. Funct. Mater. 36 (2026) e75224, https://doi.org/10.1002/adfm.75224.
[28] J. Yang, Y. Shen, J. Xian, R. Xiang, G. Li, Rare-earth element doped NiFe-MOFs as efficient and robust bifunctional electrocatalysts for both alkaline freshwater and seawater splitting, Chem. Sci. 16 (2025) 685–692, https://doi.org/10.1039/D4SC06574C.
[29] S. Muhammad, L. Wang, Z. Huang, A. Zhou, H. Bilal, T. Taylor Isimjan, X. Yang, Recent advances in lanthanide-based materials for oxygen evolution reaction: Challenges and future prospects, Coord. Chem. Rev. 534 (2025) 216573, https://doi.org/10.1016/j.ccr.2025.216573.
[30] Y. Liao, Y. Xiao, Z. Li, X. Zhou, J. Liu, F. Guo, J. Li, Y. Li, Structural engineering of Co-metal–organic frameworks via Ce incorporation for improved oxygen evolution, Small 20 (2024) 2307685, https://doi.org/10.1002/smll.202307685.
[31] Y. Ma, G.-M. Mu, Y.-J. Miao, D.-M. Lin, C.-G. Xu, F.-Y. Xie, W. Zeng, Hydrangea flower-like nanostructure of dysprosium-doped Fe-MOF for highly efficient oxygen evolution reaction, Rare Met. 41 (2022) 844–850, https://doi.org/10.1007/s12598-021-01851-9.
[32] T.R. Whitfield, X. Wang, L. Liu, A.J. Jacobson, Metal-organic frameworks based on iron oxide octahedral chains connected by benzenedicarboxylate dianions, Solid. State Sci. 7 (2005) 1096–1103, https://doi.org/10.1016/j.solidstatesciences.2005.03.007.
[33] J. Joseph, S. Iftekhar, V. Srivastava, Z. Fallah, E.N. Zare, M. Sillanpää, Iron-based metal-organic framework: Synthesis, structure and current technologies for water reclamation with deep insight into framework integrity, Chemosphere 284 (2021) 131171, https://doi.org/10.1016/j.chemosphere.2021.131171.
[34] X. Cao, L. Miao, W. Jia, H. Qin, G. Lin, R. Ma, T. Jin, L. Jiao, Strain heterogeneity in RuO_2 for efficient acidic oxygen evolution reaction in proton exchange membrane water electrolysis, Nat. Commun. 16 (2025) 6217, https://doi.org/10.1038/s41467-025-58570-3.
[35] L. Miao, W. Jia, X. Cao, L. Jiao, Computational chemistry for water-splitting electrocatalysis, Chem. Soc. Rev. 53 (2024) 2771–2807, https://doi.org/10.1039/D2CS01068B.
[36] M. Kaiser, Effect of lanthanide and transition metal on the structure, magnetic, and electric properties of nickel ferrites, Appl. Phys. A 129 (2023) 840, https://doi.org/10.1007/s00339-023-07082-2.
[37] B. Tan, Z.-F. Wu, X.-Y. Huang, An Iron-NDC Framework with a Cage Structure and an Optothermal Conversion in NIR Window, Molecules 27 (2022) 8789, https://doi.org/10.3390/molecules27248789.
[38] V. Singh, D.K. Singh, M. Yadav, S. Singh, V. Rathour, A. Tiwari, V. Ganesan, A Co and Fe bimetallic MOF with enhanced electrocatalytic oxygen evolution performance: exploring the electronic environment modifications upon Fe incorporation, Energy Adv. 3 (2024) 636–647, https://doi.org/10.1039/D3YA00572K.
[39] J. Liu, L. He, Z. Tao, S. Li, C. Wang, Y. Zhang, S. Zhang, M. Du, Z. Zhang, Ferric Oxide Nanocrystals-Embedded Co/Fe-MOF with Self-Tuned d-Band Centers for Boosting Urea-Assisted Overall Water Splitting, Small 20 (2024) 2306273, https://doi.org/10.1002/smll.202306273.
[40] Y. Li, L.X. Song, W.P. Wang, Y. Teng, J. Xia, N.N. Liu, Controlled Morphological Transformation, Photocatalytic Properties, and Electrocatalytic OER Performance of Fe-MOF Nanopolyhedra, J. Phys. Chem. C. 125 (2021) 27207–27220, https://doi.org/10.1021/acs.jpcc.1c07710.
[41] W. Liu, C. Ni, M. Gao, X. Zhao, W. Zhang, R. Li, K. Zhou, Metal–Organic-Framework-Based Nanoarrays for Oxygen Evolution Electrocatalysis, ACS Nano 17 (2023) 24564–24592, https://doi.org/10.1021/acsnano.3c09261.
[42] Q. Zha, M. Li, Z. Liu, Y. Ni, Hierarchical Co,Fe-MOF-74/Co/Carbon Cloth Hybrid Electrode: Simple Construction and Enhanced Catalytic Performance in Full Water Splitting, ACS Sustain. Chem. Eng. 8 (2020) 12025–12035, https://doi.org/10.1021/acssuschemeng.0c02993.
[43] L. Xiao, X. Bai, J. Han, T. Tang, S. Chen, H. Qi, C. Hou, F. Bai, Z. Wang, J. Guan, Surface reconstruction and structural transformation of two-dimensional Ni-Fe MOFs for oxygen evolution in seawater media, Nano Res. 17 (2024) 2429–2437, https://doi.org/10.1007/s12274-023-6088-x.
[44] Q. Qi, J. Hu, Y. Zhang, W. Li, B. Huang, C. Zhang, Two-Dimensional Metal–Organic Frameworks-Based Electrocatalysts for Oxygen Evolution and Oxygen Reduction Reactions, Adv. Energy Sustain. Res. 2 (2021) 2000067, https://doi.org/10.1002/aesr.202000067.
[45] L. Liu, D. Zhang, Y. Zhu, Y. Han, Bulk and local structures of metal–organic frameworks unravelled by high-resolution electron microscopy, Comm. Chem. 3 (2020) 99, https://doi.org/10.1038/s42004-020-00361-6.
[46] K.C. Devarayapalli, S.V.P. Vattikuti, T.V.M. Sreekanth, K.S. Yoo, P.C. Nagajyothi, J. Shim, Hydrogen production and photocatalytic activity of g-C_3N_4/Co-MOF (ZIF-67) nanocomposite under visible light irradiation, Appl. Organo Chem. 34 (2020) e5376, https://doi.org/10.1002/aoc.5376.
[47] C. Sharma, N. Sharma, S. Sharma, S. Sharma, S. Paul, Nano-rod like morphology of Ni@Fe_3O_4-NDCs on interaction of NDC-supported Fe_3O_4 with nickel NPs: An efficient catalyst for ligand free Chan-Lam coupling reaction in aqueous medium, Curr. Res. Green. Sustain. Chem. 4 (2021) 100133, https://doi.org/10.1016/j.crgsc.2021.100133.
[48] A.E. Rashed, M.S. Nofal, A.A. El-Moneim, Thermally stable metal–organic framework based iron 2,6-naphthalenedicarboxylic catalyst (Fe-NDC) for syngas conversion to olefin, Sci. Rep. 15 (2025) 26526, https://doi.org/10.1038/s41598-025-09332-0.
[49] Y. Wang, W. Tang, X. Li, D. Wei, Improving the electrocatalytic activity of NiFe bimetal-organic framework toward oxygen evolution reaction by Zr doping, Electrochim. Acta 381 (2021) 138292, https://doi.org/10.1016/j.electacta.2021.138292.
[50] S. Ding, Y. Zhang, F. Lou, M.K. Aslam, Y. Sun, M. Li, J. Duan, Y. Li, S. Chen, Uncapped" metal–organic framework (MOF) dispersions driven by O_2 plasma towards superior oxygen evolution electrocatalysis, J. Mater. Chem. A 10 (2022) 20813–20818, https://doi.org/10.1039/D2TA05387J.
[51] L. Yu, Z. Nie, S. Xie, L. Jiang, B. Xia, M. Li, C. Cheng, J. Duan, M. Antonietti, S. Chen, Bioinspired inhibition of aggregation in metal-organic frameworks (MOFs), iScience 26 (2023) 106239, https://doi.org/10.1016/j.isci.2023.106239.
[52] S. Zhao, Y. Wang, Y. Hao, L. Yin, C.H. Kuo, H.Y. Chen, L. Li, S. Peng, Lewis acid driving asymmetric interfacial electron distribution to stabilize active species for efficient neutral water oxidation, Adv. Mater. 36 (2024) 2308925, https://doi.org/10.1002/adma.202308925.
[53] C. Fang, X. Tang, Q. Yi, Adding Fe/dicyandiamide to Co-MOF to greatly improve its ORR/OER bifunctional electrocatalytic activity, Appl. Catal. B Environ. Energy 341 (2024) 123346, https://doi.org/10.1016/j.apcatb.2023.123346.
[54] S.M. Suresh, D.R.G. Ravinandana, S.B. Prasanna, S.M. Basavaraju, K.M. Basavaraju, C.S. Rout, S.M. Ankanathappa, R.-J. Chung, N.P.H. Shivabasappa, Cubic mesoporous Fe–Zn MOF@CNT hybrid: a high-efficiency bifunctional electrocatalyst for water splitting, J. Porous Mater. 33 (2026) 743–759, https://doi.org/10.1007/s10934-025-01910-x.
[55] A.M. Shaiful Bahari, S.Z. Othman, M.F. Mohamad Fadli, M.Z.A. Zulkifli, S. A. Biyamin, M.A. Islam, Z. Aspanut, N. Amin, H. Misran, Facile synthesis of Zr-based metal-organic gel (Zr-MOG) using "green" sol-gel approach, Surf. Interfaces 27 (2021) 101469, https://doi.org/10.1016/j.surfin.2021.101469.
[56] X. Mao, J. Zhou, J. Wu, S. Chen, P. Wang, Y. You, Novel Polyarylene Ether Nitrile/$BaTiO_3$-Decorated WS_2 Nanohybrid Crosslinked Nanocomposites for Thermal-Stable Dielectrics, Polymers 18 (2026) 747, https://doi.org/10.3390/polym18060747.

[57] N. Dubey, S. Gupta, S.B. Shelar, K.C. Barick, S. Chandra, Maximizing Upconversion Luminescence of Co-Doped CaF_2:Yb, Er Nanoparticles at Low Laser Power for Efficient Cellular Imaging, Molecules 29 (2024) 4177, https://doi.org/10.3390/molecules29174177.
[58] A. Sarilmaz, Ytterbium oxide nanofibers: fabrication and characterization for energy applications, Turk. J. Chem. 46 (2022) 1694–1701, https://doi.org/10.55730/1300-0527.3472.
[59] F. Wei, J. Shen, Z. Luo, P. Sun, H. Liu, X. Shi, B. Liu, X. Yang, D. Cao, Z. Wang, Y. Zhu, B. Wu, Lewis acid-mediating local alkaline microenvironment for efficient oxygen evolution, Appl. Catal. B Environ. Energy 394 (2026) 126821, https://doi.org/10.1016/j.apcatb.2026.126821.
[60] X. Cao, H. Qin, J. Zhang, X. Chen, L. Jiao, Regulation of Oxide Pathway Mechanism for Sustainable Acidic Water Oxidation, J. Am. Chem. Soc. 146 (2024) 32049–32058, https://doi.org/10.1021/jacs.4c12942.
[61] W. Jia, L. Miao, X. Cao, X. Chen, T. Jin, F. Cheng, L. Jiao, J. Chen, Manganese-containing electrocatalysts for sustainable acidic oxygen evolution, eScience 6 (2026) 100427, https://doi.org/10.1016/j.esci.2025.100427.
[62] H. Li, J. Xu, L. Yang, W. Wang, B. Shao, F. Cheng, C. Zhao, W. Wang, Advancing Mn-based electrocatalysts: Evolving from Mn-centered octahedral entities to bulk forms, eScience 5 (2025) 100368, https://doi.org/10.1016/j.esci.2024.100368.
[63] C. Ling, X. Leng, X.-J. Lu, J.-H. Li, Z. Yang, A.-W. Xu, A self-supported S-doped Fe-based organic framework platform enhances electrocatalysis toward highly efficient oxygen evolution in alkaline media, J. Mater. Chem. A 10 (2022) 17246–17253, https://doi.org/10.1039/D2TA04857D.
[64] S. Muhammad, B. Yao, A. Zhou, Z. Huang, S. Khan, F. Wei, Z. Luo, T.T. Isimjan, X. Yang, Unveiling dynamic surface transformations: Mo-doped Fe-based MOFs as next-generation oxygen evolution catalysts, Green. Chem. 27 (2025) 5554–5566, https://doi.org/10.1039/D5GC01263E.
[65] Y. Ma, G.-M. Mu, Y.-J. Miao, D.-M. Lin, C.-G. Xu, F.-Y. Xie, W. Zeng, Hydrangea flower-like nanostructure of dysprosium-doped Fe-MOF for highly efficient oxygen evolution reaction, Rare Met. 41 (2022) 844–850, https://doi.org/10.1007/s12598-021-01851-9.
[66] M. Burud, S.A. Patil, V. Jadhav, P. Chougale, S. Mane-Gavade, R. Ustad, J. Shen, A. Supale, S. Sabale, D.-K. Kim, Synergistic Effect of CoFe Bimetallic MOF for Efficient Electrocatalytic OER in Alkaline Media, Energy Fuels 39 (2025) 13648–13657, https://doi.org/10.1021/acs.energyfuels.5c01134.
[67] X. Zhang, S. Chen, K. Wang, Z. Tang, X. Wang, The In-situ preparation of CoFe LDH/MOF electrocatalysts with 2D/2D structure and its enhanced electrocatalytic performance for OER, Electrochim. Acta 548 (2026) 147946, https://doi.org/10.1016/j.electacta.2025.147946.
[68] X. Mu, M. Yu, X. Liu, Y. Liao, F. Chen, H. Pan, Z. Chen, S. Liu, D. Wang, S. Mu, High-Entropy Ultrathin Amorphous Metal–Organic Framework-Stabilized Ru(Mo) Dual-Atom Sites for Water Oxidation, ACS Energy Lett. 9 (2024) 5763–5770, https://doi.org/10.1021/acsenergylett.4c02552.
[69] K. Ding, J. Hu, L. Zhao, W. Jin, H. Yu, Y. Liu, Z. Wu, S. Cai, Y. Yang, G. Zou, H. Hou, X. Ji, Physical upcycling of spent artificial diamond accelerant into bifunctional oxygen electrocatalyst with dual-metal active sites for durable rechargeable Zn–air batteries, Nano Energy 121 (2024) 109270, https://doi.org/10.1016/j.nanoen.2024.109270.
[70] S. Zhang, Z. Huang, T.T. Isimjan, D. Cai, X. Yang, Accurately substituting Fe for Ni_2 atom in Ni-MOF with defect-rich for efficient oxygen evolution reaction: Electronic reconfiguration and mechanistic study, Appl. Catal. B Environ. Energy 343 (2024) 123448, https://doi.org/10.1016/j.apcatb.2023.123448.
[71] L. Huang, G. Gao, H. Zhang, J. Chen, Y. Fang, S. Dong, Self-dissociation-assembly of ultrathin metal-organic framework nanosheet arrays for efficient oxygen evolution, Nano Energy 68 (2020) 104296, https://doi.org/10.1016/j.nanoen.2019.104296.
[72] X. Liu, R. Guo, W. Huang, J. Zhu, B. Wen, L. Mai, Advances in Understanding the Electrocatalytic Reconstruction Chemistry of Coordination Compounds, Small 17 (2021) 2100629, https://doi.org/10.1002/smll.202100629.
[73] T.A. Zegeye, W.-T. Chen, C.-C. Hsu, J.A.A. Valinton, C.-H. Chen, Activation Energy Assessing Potential-Dependent Activities and Site Reconstruction for Oxygen Evolution, ACS Energy Lett. 7 (2022) 2236–2243, https://doi.org/10.1021/acsenergylett.2c01103.
[74] X. Luo, H. Zhao, X. Tan, S. Lin, K. Yu, X. Mu, Z. Tao, P. Ji, S. Mu, Fe-S dually modulated adsorbate evolution and lattice oxygen compatible mechanism for water oxidation, Nat. Commun. 15 (2024) 8293, https://doi.org/10.1038/s41467-024-52682-y.
[75] F. He, E. Gillette, X. Wang, A. Huxford, C. Xiao, Y. Yan, M.C. Beard, J. Gu, Spin-Polarized Oxygen Evolution Reaction Enabled by Chiral Molecules Coupled with Ferromagnetic Electrocatalysts, ACS Appl. Mater. Interfaces 17 (2025) 69389–69397, https://doi.org/10.1021/acsami.5c18273.
[76] L.-H. Yu, Z.-M. Ye, X.-F. Zhang, H.-G. Du, L.-D. Wang, M.-T. Zhang, J. Yang, J. Zhang, L.-M. Cao, C.-T. He, Decoupling the Electronic and Steric Effects on All-Organic Electrocatalysts for Direct Oxygen Evolution Reaction, Adv. Funct. Mater. 36 (2026) e18505, https://doi.org/10.1002/adfm.202518505.
[77] N. Yao, H. Jia, J. Zhu, Z. Shi, H. Cong, J. Ge, W. Luo, Atomically dispersed Ru oxide catalyst with lattice oxygen participation for efficient acidic water oxidation, Chem 9 (2023) 1882–1896, https://doi.org/10.1016/j.chempr.2023.03.005.
[78] Y. Wang, L. Zhao, J. Ma, J. Zhang, Confined interface transformation of metal–organic frameworks for highly efficient oxygen evolution reactions, Energy Environ. Sci. 15 (2022) 3830–3841, https://doi.org/10.1039/D2EE01073A.
[79] G. Wang, C. Chi, Y. Zhou, B. Mu, Q. Miao, B. Qi, X. Yang, F. Feng, L. Wu, X. Zhao, Y. Huang, C. Wang, T. Wei, Z. Fan, Activating the oxide pathway mechanism via selective intralayer Cl coordination with Ni/Fe sites of hydroxides for robust water oxidation, Energy Environ. Sci. 19 (2026) 2668–2678, https://doi.org/10.1039/D5EE07316B.
[80] Z. Zeb, Y. Huang, L. Chen, R. Gao, X. Gao, M. Sun, H. Cai, J. Chen, F. Abbas, M. Liao, L. Ni, Y. Wei, Polyoxometalates metal–organic frameworks-derived transition metal sulfides with rich interfaces for efficient alkaline oxygen evolution reaction, J. Colloid Interface Sci. 686 (2025) 289–303, https://doi.org/10.1016/j.jcis.2025.01.221.
[81] Z. Zou, T. Wang, X. Zhao, W.-J. Jiang, H. Pan, D. Gao, C. Xu, Expediting in-Situ Electrochemical Activation of Two-Dimensional Metal–Organic Frameworks for Enhanced OER Intrinsic Activity by Iron Incorporation, ACS Catal. 9 (2019) 7356–7364, https://doi.org/10.1021/acscatal.9b00072.
[82] J. Song, R.K. Chitumalla, M.H. Kim, J. Jang, D. Jin, Perturbing d-band center via high-entropy modulation within spinel lattices toward enhanced oxygen evolution reaction catalysis, Nano Energy 148 (2026) 111632, https://doi.org/10.1016/j.nanoen.2025.111632.
[83] H. Jia, N. Yao, Y. Jin, L. Wu, J. Zhu, W. Luo, Stabilizing atomic Ru species in conjugated sp^2 carbon-linked covalent organic framework for acidic water oxidation, Nat. Commun. 15 (2024) 5419, https://doi.org/10.1038/s41467-024-49834-5.
[84] Y. Wu, Y. Gan, L. Wen, Y. Ye, R. Cai, B. Wang, Y. Song, S. Qiao, Q. Jiang, X. Niu, X. Dai, X. Zhang, Superhydrophilic La-doped NiFe LDH Heterostructure facilitating lattice oxygen mechanism for efficient water/seawater electrolysis, Chem. Eng. J. 535 (2026) 175271, https://doi.org/10.1016/j.cej.2026.175271.
[85] Y. Liao, Y. Xiao, Z. Li, X. Zhou, J. Liu, F. Guo, J. Li, Y. Li, Structural Engineering of Co-Metal–Organic Frameworks via Ce Incorporation for Improved Oxygen Evolution, Small 20 (2024) 2307685, https://doi.org/10.1002/smll.202307685.
[86] F. Zhang, Q. Liu, L. Ma, S. Wu, M. Yan, X. Meng, B. Chen, W. Wang, L. Chen, Z. Wei, D. Jia, Y. Zhou, W. Sun, X. Duan, Ce-doping optimized interface synergy in Co-Ce alloy/NiFe layered double hydroxide/carbon fiber paper heterostructure for boosted oxygen evolution reaction, Colloids Surf. A Physicochem. Eng. Asp. 745 (2026) 140685, https://doi.org/10.1016/j.colsurfa.2026.140685.
[87] Z. Gao, B. Liu, X. Xu, J. Peng, J. Wu, J. Zhang, Electrochemical oxidation induced in-situ transformation of lamellar cobalt nitrate-hydroxide to oxygen vacancy-rich porous Ce Doped-CoOOH nanosheet for efficient oxygen evolution reaction, Mater. Today Sustain. 24 (2023) 100601, https://doi.org/10.1016/j.mtsust.2023.100601.
[88] S. Ma, X. Wang, Z. Hu, Y. Cao, X. Zhang, S. Shi, P. Yang, H. Jiang, Y. Han, H. Zhang, Fe-doping promotes surface reconstruction and electronic modulation of Ni-MOF enabling industrial-current-density oxygen evolution, J. Alloy. Compd. 1051 (2026) 185958, https://doi.org/10.1016/j.jallcom.2026.185958.
[89] Y. Hao, S.-F. Hung, W.-J. Zeng, Y. Wang, C. Zhang, C.-H. Kuo, L. Wang, S. Zhao, Y. Zhang, H.-Y. Chen, S. Peng, Switching the Oxygen Evolution Mechanism on Atomically Dispersed Ru for Enhanced Acidic Reaction Kinetics, J. Am. Chem. Soc. 145 (2023) 23659–23669, https://doi.org/10.1021/jacs.3c07777.